Научном већу Института за физику у Београду

Београд, 20.9.2024.

Предмет: Молба за покретање поступка за избор у звање истраживач сарадник

Молим научно веће Института за физику у Београду да покрене поступак за мој избор у звање истраживач сарадник.

У прилогу достављам:

1. Мишљење руководиоца лабораторије са предлогом чланова комисије за избор у звање
2. Стручну биографију
3. Преглед научне активности
4. Списак објављених научних радова и њихове копије
5. Потврду о уписаним докторским студијама
6. Копију диплома основних и мастер студија
7. Одлука о одобреној теми докторске дисертације

Са поштовањем,

Алекса Денчевски

Истраживач приправник

НАУЧНОМ ВЕЋУ ИНСТИТУТА ЗА ФИЗИКУ У БЕОГРАДУ

Предмет: Мишљење руководиоца лабораторије о избору Алексе Денчевског у звање истраживач сарадник

Алекса Денчевски, мастер физичар, је запослен у Лабораторији за биофизику у оквиру Центра за фотонику. Студнет је докторских студија из Биофизике при Универзитету у Београду. Докторску дисертацију из области супер резолуционих микроскопских техника ради под руководством др Иване Древнице, вишег научног сарадника запослене у Институту за медицинска истраживања у Београду и др Михаила Рабасовића, вишег научног сарадника запосленог у Институту за физику у Београду.

С обзиром да испуњава предвиђене услове прописане Законом о науци и истраживањима и Правилником о стицању научних и истраживачких звања Министарства науке, технолошког развоја и иновација, сагласан сам да Научно веће Института за физику у Београду покрене поступак за избор Алексе Денчевског у звање истраживач сарадник.

Предлажем да комисију за избор Алексе Денчевског у звање истраживач сарадник чине:

1. др Михаило Рабасовић, виши научни сарадник, Институт за физику у Београду.
2. др Ивана Дрвеница, виши научни сарадник, Институт за медицинска истраживања у Београду
3. др Марко Николић, виши научни сарадник, Институт за физику у Београду

У Београду,
12. IX 2024.

Руководилац лабораторије,

др Александар Крмпот
научни саветник
Институт за физику

2. Стручна биографија

Алекса Денчевски је рођен 24. фебруара 1998. године у Краљеву. Основне студије, на Физичком факултету у Београду на смеру Примењена и компјутерска физика уписује 2016. године. Дипломирао је 2020. године, док је мастер студије на истом смеру завршио 2021. године са темом „Карактеризација и синхронизација побудног, управљачког и детекционог система микроскопа са структурисаним просвертљавањем“. Након завршетка мастер студија уписује мултидисциплинарне докторске студије Биофизике при Универзитету у Београду. Од децембра 2021. године Алекса Денчевски је запослен у Институту за физику у Београду као истраживач приправник у Лабораторији за биофизику у Центру за фотонику. На седници ИМТ већа Универзитета у Београду која је одржана 10.07.2024. године, одобрена је тема његове докторске дисертације под насловом **„Развој суперрезолуционог микроскопа са структурисаним просветљавањем за изучавање морфолошких промена еритроцита“**, а за менторе су одређени др Михаило Рабасовић (Институт за физику у Београду, Универзитет у Београду) и др Ивана Дрвеница (Институт за медицинска истраживања, Универзитет у Београду). Од јануара 2024. године Алекса Денчевски учествује на MSCA RISE пројекту ULTIMATE-I (grant ID 101007825) као члан пројектног тима из Србије. Поред тога, Алекса Денчевски је учествовао на пројекту „Integrating Picosecond Excitation for Dynamic Fluorescence Analysis“ у оквиру SEED интерног позива Института за физику у Београду. Алекса Денчевски координише Лабораторијом за физику и електронику Истраживачке станце Петница, где поред организационих активности менторише и велики број експерименталних пројеката.

3. Преглед научне активности

Научно истраживачки рад Алексе Денчевског обухвата експериментално истраживање у области развоја и примене суперрезолуционе микроскопије. Алекса Денчевски је свој научно истраживачки рад започео током мастер студија на којима је радио карактеризацију и синхронизацију дела система микроскопа са структурисаним просветњавањем (*Structured Illumination Microscopy - SIM*). Након завршених мастер студија наставља истраживање и развија потпуно функционалан суперрезолуциони микроскоп на ком снима прве флуоресцентно обележене биолошке узорке и развија методе директног мерења резолуције. Развој и примена микроскопа са структурисаним просветљавањем су предмет његове докторске дицертације. Очекивани научни допринос његове докторске дисератације огледа се у новој метологији развоја суперрезолуционог микроскопа са структурисаним просветљавањем која користи методу микрофилмовања трансмисионих дифракционих решетки. Овакав микроскоп се користи за снимање различитих биолошких узорака, а резултати снимања субструктура омогућавају боље разумевање билошки релеватних процеса. У његовој дисертацији биће идентификоване и квантификоване морфолошке абнормалности који су у вези са функционалним поремећајима еритроцита. До сада, Алекса Денчевски има један рад објављен у часопису категорије М21, један рад објављен у часопису категорије М22 и један рад објављен у категорији М23 као и неколико саопштења са међународних скупова и скупова националног значаја.

4. Списак објављених научних радова и њихове копије

4.1.Радови у врхунским међународним часописима (М21)

Jovana Z Jelić, Marta Bukumira, **Aleksa Denčevski**, Ana Senkić, Livio Žužić, Borna Radatović, Nataša Vujičić, Tanja Pajić, Mihailo D Rabasović, Aleksandar J Krmpot, Application of the Knife-Edge Technique on Transition Metal Dichalcogenide Monolayers for Resolution Assessment of Nonlinear Microscopy Modalities, *Microscopy and Microanalysis*, 2024, https://doi.org/10.1093/mam/ozae061

4.2.Радови у истакнутим међународним часописима (М22)

Jovana Z. Jelić, **Aleksa Denčevski**, Mihailo D. Rabasović, Janez Krizan, Svetlana Savić-Šević, Marko G. Nikolić, Miryam H. Aguirre, Dragutin Šević, Maja S. Rabasović, Improving the Two-Color Temperature Sensing Using Machine Learning Approach: $GdVO_4:Sm^{3+}$ Prepared by Solution Combustion Synthesis (SCS), *Photonics* **2024**, *11*, 642. https://doi.org/10.3390/photonics11070642.

4.3.Радови у међународним часописима (М23)

Maja S. Rabasović, **Aleksa Denčevski**, Mihailo D. Rabasović, Dragutin M. Šević, Data of plasma velocity obtained from Streak image processing of laser-induced breakdown, Contributions of the Astronomical Observatory Skalnaté Pleso, vol. 53, no. 3, p. 115-124. doi.org/10.31577/caosp.2023.53.3.115

4.4.Саопштења са међународних скупова штампана у изводу (М34)

Marta Bukumira, Jovana Z. Jelić, **Aleksa Denčevski**, Mihailo D. Rabasović, Nataša Vujičić, Ana Senklić, Antonio Supina, Aleksandar J. Krmpot, Determination of spatial resolution of nonlinear laser scanning microscopy, 11th International Conference of the Balkan Physical Union, Belgrade, Serbia (BPU11), ISBN: 978-86-7025-950-8

Aleksa Denčevski, Aleksandar J. Krmpot, Mihailo D. Rabasović, Development of two-dimensional superresolution fluorescence microscope with structured illumination, Photonica 2023, Belgrade, Serbia, ISBN: 978-86-7306-168-9

Marta Bukumira, Jovana Z. Jelić, **Aleksa Denčevski**, Mihailo D. Rabasović, Nataša Vujičić, Ana Senklić, Antonio Supina, Aleksandar J. Krmpot, Cutting edge technique for determination of spatial resolution limits of nonlinear laser scanning microscopy, Photonica 2023, Belgrade, Serbia, ISBN: 978-86-7306-168-9

Jovana Z. Jelić, **Aleksa Denčevski**, Mihailo D. Rabasović, Aleksandar J. Krmpot, Quantitative measurement of concentration and diffusion properties of molecules using fluorescence correlation spectroscopy, IAPC 10, Belgrade, Serbia

4.5.Саопштење са скупа националног значаја штампано у изводу (М64)

Марта Букумира, Станко Николић, Јована Јелић, **Алекса Денчевски**, Михаило Рабасовић, Наташа Вујичић, Ана Сенкић, Антонио Супина, Александар Крмпот,

Одређивање граница просторне резолуције нелинеарне ласерске скенирајуће микроскопије, Конгрес биолога Србије (Септембар 2022., Златибор, ISBN: 978-86-81413-09-8)

Microscopy and Microanalysis, 2024, **30**, 671–680
https://doi.org/10.1093/mam/ozae061
Advance access publication 12 July 2024
Original Article

Microscopy AND Microanalysis

Application of the Knife-Edge Technique on Transition Metal Dichalcogenide Monolayers for Resolution Assessment of Nonlinear Microscopy Modalities

Jovana Z. Jelić[1], Marta Bukumira[1], Aleksa Denčevski[1], Ana Senkić[2], Livio Žužić[3], Borna Radatović[4], Nataša Vujičić[2], Tanja Pajić[5], Mihailo D. Rabasović[1], and Aleksandar J. Krmpot[1,*]

[1]*Institute of Physics Belgrade, University of Belgrade, National Institute of the Republic of Serbia, Pregrevica 118, Belgrade 11080, Serbia*
[2]*Centre for Advanced Laser Techniques, Institute of Physics Zagreb, Bijenička cesta 46, Zagreb 10000, Croatia*
[3]*Department of Physics, University of Zagreb, Bijenička cesta 32, Zagreb 10000, Croatia*
[4]*Materials Science Factory, Instituto de Ciencia de Materiales de Madrid (ICMM-CSIC), Sor Juana Ines de la Cruz 3, Madrid 28049, Spain*
[5]*Department for General Physiology and Biophysics, Faculty of Biology, University of Belgrade, Studentski trg 16, Belgrade, 11158, Serbia*

***Corresponding author:** Aleksandar J. Krmpot, E-mail: krmpot@ipb.ac.rs

Abstract

We report application of the knife-edge technique at the sharp edges of WS_2 and MoS_2 monolayer flakes for lateral and axial resolution assessment in all three modalities of nonlinear laser scanning microscopy: two-photon excited fluorescence (TPEF), second- and third-harmonic generation (SHG, THG) imaging. This technique provides a high signal-to-noise ratio, no photobleaching effect and shows good agreement with standard resolution measurement techniques. Furthermore, we assessed both the lateral resolution in TPEF imaging modality and the axial resolution in SHG and THG imaging modality directly via the full-width at half maximum parameter of the corresponding Gaussian distribution. We comprehensively analyzed the factors influencing the resolution, such as the numerical aperture, the excitation wavelength and the refractive index of the embedding medium for the different imaging modalities. Glycerin was identified as the optimal embedding medium for achieving resolutions closest to the theoretical limit. The proposed use of WS_2 and MoS_2 monolayer flakes emerged as promising tools for characterization of nonlinear imaging systems.

Key words: knife-edge technique, nonlinear laser scanning microscopy, resolution measurement, second/third harmonic generation, WS_2 and MoS_2 monolayers

Introduction

Nonlinear laser scanning microscopy (NLSM) is a specialized microscopy technique that uses localized nonlinear excitation to excite fluorescence only within a thin raster-scanned plane. In NLSM, two-photon excited fluorescence (TPEF) is typically detected and used for imaging (Masters & So, 2009; Tserevelakis et al., 2012; Rohrbacher et al., 2017). In addition to TPEF, other imaging techniques include three-photon excited fluorescence, and second- and third-harmonic generation (SHG, THG) (Zipfel et al., 2003; Tserevelakis et al., 2010).

Every optical system has a fundamental limitation of resolution due to diffraction which causes the image to spread in both lateral and axial directions. The diffraction pattern (light intensity distribution) of a point-like light source in the lateral (x,y) and axial (z) dimensions is referred to as a point-spread function (PSF) (Cole et al., 2011). According to the Houston criterion for resolution (van den Bos & den Dekker, 2001), two point sources are considered resolved if the full-width at half maximum (FWHM) of their PSFs no longer overlap. In microscopy, resolution depends on many factors such as numerical aperture (NA) of the objective lens, wavelength, refractive index of the embedding medium, coverglass thickness, distance between the object and coverglass, etc. (Kozubek, 2001).

The standard technique for evaluating resolution is based on the imaging of nanospheres, often referred to as beads. Beads can be used directly to assess lateral resolution, or to determine the PSF by applying the deconvolution method (using bead images and prior knowledge of the actual bead size). Although this method is practical, it does have certain limitations. As bead size decreases, the signal-to-noise ratio (SNR) deteriorates, making it challenging to obtain reliable measurements. Deconvolution, on the other hand, can be severely affected by noise. With axial resolution, the stack image of the beads must be recorded. This is challenging in practice as the beads are prone to photobleaching. Consequently, the measurement of axial resolution results in a relatively small number of data points which affects the quality of the assessment. Furthermore, due to the coherent nature of the SHG signal, its PSF is a contentious issue, as pointed out in Chen et al. (2012). Accordingly, imaging of common polystyrene beads by SHG microscopy is not widely used and has been reported only in terms of the material nonlinear response characterization, with no resolution assessment (Hou & Labarthet, 2018). Similarly, sparse THG imaging of similar objects for resolution measurement was demonstrated in Masihzadeh et al. (2009). Several inorganic nanocrystals of noble metals or metal oxides arranged in a noncentrosymmetric crystal structure

Received: February 5, 2024. **Revised:** June 19, 2024. **Accepted:** June 23, 2024

(such as $KTiOPO_4$) have been used as point-like SHG signal sources in NLSM (Mahou et al., 2017), in a manner similar to beads. In contrast to fluorescence, SHG is theoretically an achromatic phenomenon which can be obtained at arbitrary wavelengths covering the entire range of tunable NIR lasers. This makes such crystal structures suitable for NLSM resolution evaluation.

Due to the lack of techniques for assessing resolution of all three modalities of NLSM (TPEF, SHG, and THG) within a single microscopic system, we were inspired to conduct a more in-depth investigation into this matter. Here, we propose application of the knife-edge technique to monolayers of transition metal dichalcogenides (TMDs), in particular WS_2 and MoS_2, for evaluation of lateral resolution. In their single-layer form, TMDs have a D_{3h} symmetry where the lack of inversion symmetry allows for an unusually strong SHG signal. This effect is very sensitive to layer thickness, crystalline orientation, and layer stacking (Kumar et al., 2013; Yin et al., 2014; Rosa et al., 2018). The thickness of our samples (<1 nm) (Radisavljevic et al., 2011) and their efficient SHG production (Woodward et al., 2016) and THG (Wang et al., 2013) signals also allow direct measurement of axial resolution. The intensity profiles obtained at the monolayer-substrate boundary are free from artifacts typically associated with thicker samples. Although a similar approach was reported by Mehravar et al. (2020), the absence of axial resolution results in their study can be attributed to excessive thickness of the samples used. Other 2D materials (2DMs) such as hBN have been reported as a test material in resolution assessment of a confocal focus-engineered coherent anti-Stokes Raman scattering (cFE-CARS) microscope (Lee et al., 2023). However, h-BN exhibits an SHG signal that is an order of magnitude lower than that of the MoS_2 monolayer (Li et al., 2013). SHG and THG signals obtained by WS_2 and MoS_2 monolayers both result in a relatively high SNR and no photobleaching effect.

While the knife-edge technique is commonly used for laser beam profile determination (Araújo et al., 2009), its application in resolution assessment of various microscopic techniques (Chu et al., 2005; Wachulak et al., 2017; Mennel et al., 2018; Mylonakis et al., 2024) has generally been limited and auxiliary. The knife-edge technique is a method of assessing resolution by analyzing the transition zone across a boundary formed by sharp-edged objects. By extracting intensity profiles across the edge and measuring the width and slope, one can determine the resolution of an optical system. A sharper and narrower transition generally indicates a higher resolution, while a wider transition indicates a lower resolution. In this study, we present the measurement of resolution in different imaging modalities of our custom-built nonlinear laser scanning microscope (Rabasovic et al., 2015) utilizing two distinct approaches.

Here, we report application of the knife-edge technique on WS_2 and MoS_2 (for lateral resolution assessment in SHG and THG modalities). We also evaluated both lateral (in TPEF modality) and axial resolution (in SHG and THG modalities) directly via the FWHM parameter of the corresponding Gaussian distribution. Our study includes a comprehensive analysis of how the resolution varies with the NA of the objective lens, excitation wavelengths, refractive index of the embedding medium, and imaging modality of the microscope. In addition, the obtained PSF (FWHM) values were employed in deconvolution of the image, resulting in significant improvement in image resolution.

Materials and Methods

NLSM Experimental Setup

Our custom-made NLSM system [detailed information can be found in Pajić et al. 2022] enables precise control of power levels and motorized positioning of the sample in the axial direction with a minimum step-size of 0.25 μm. For TPEF and SHG imaging, a tunable (700–1,000 nm) Kerr lens mode-locked femtosecond Ti: Sapphire laser (Mira 900, Coherent Inc., CA, USA) with a repetition rate of 76 MHz and pulse duration of 160 fs was used. Femtosecond pulses were also obtained from a SESAM mode-locked Yb:KGW laser (Time-Bandwidth Products AG, Time-Bandwidth Yb GLX; Zurich, Switzerland) at a fixed wavelength of 1,040 nm with a pulse duration of 200 fs and a repetition rate of 83 MHz. After being expanded 3.75 times with a Keplerian telescope (obtained by AC254-040-A and AC254- 150-A lenses, both from Thorlabs, Inc.), the laser beams are directed toward the objective lens via a main dichroic mirror (MDM; FF700-SDi01-25x36, Semrock). Beam raster scanning over the sample is achieved using a galvo scanner (6,215H, Cambridge Technologies). A National Instruments USB-6351 card was used for signal acquisition and control of the galvo scanner with a sampling rate of 1.2 M sample/s.

SHG and TPEF signals were collected in back reflection by an objective lens, passed through the MDM, filtered with appropriate filters (depending on the excitation wavelengths used and imaging modality), and then focused onto a photomultiplier tube (PMT) (RCA, PF10006). In SHG modality, we used several narrow bandpass filters (FBH370-10, FBH400-10, FBH420-10, and FB520-10, all from Thorlabs, Inc.). In the TPEF modality, the signal was filtered with a shortpass filter (FESH0700, Tholarbs, Inc.). In THG imaging, the signal was detected in the forward direction (transmission arm) after being reflected by two harmonic beam splitters (HBSY13, Thorlabs, Inc.) to reduce reflection of laser light. Finally, the residual laser light was filtered out by two filters (FGUV11M, Thorlabs, Inc. and FSR-U340, Newport). After filtering, the THG signal was focused onto the entrance window of the PMT (H7422, Hamamatsu, Japan).

Fluorescent Beads

To measure lateral resolution in TPEF modality, we used a TetraSpeck Fluorescent Microspheres Size Kit (Invitrogen, Thermo Fisher Scientific Inc.) which was specially developed for the calibration of microscopes. The slide contains six viewing areas, each of which contains nanospheres of a specific (nominal) size: 0.1 μm, 0.2 μm, 0.5 μm, 1.0 μm, or 4.0 μm and a mixture of all sizes. Each nanosphere is stained with four different fluorescent dyes: 365/430 nm, 505/515 nm, 560/580 nm, and 660/680 nm. This makes them suitable for applications that require a broad spectral range. For the purpose of resolution measurements, the optimal SNR was obtained for 0.2 μm fluorescent beads. The profile extracted from the recorded images of the beads was fitted by the Gaussian function. The lateral resolution was directly assessed through the FWHM parameter of the Gaussian fit.

WS_2 and MoS_2 Monolayers

Synthesis

MoS_2 samples were synthesized using a chemical vapor deposition (CVD) technique, described in detail in Senkić et al. (2023). Samples were grown on two substrates: c-cut sapphire

and Si/SiO_2, each with a 290 nm oxide layer thickness. The synthesis procedure is the same as described in Senkić et al. (2023), with a growth temperature, T_G, equal to 875°C. The thickness of monolayers was determined using atomic force microscopy (AFM), and was determined to be 0.8 nm Senkić et al. (2023).

Similar to the MoS_2 growth, DI water-based solutions were used for WS_2. As a growth promotor, a 5 ppm concentration of NaOH solution was used, whereas the tungsten source was a 100 ppm concentration of ammonium metatungstate hydrate $(NH_4)_6H_2W_{12}O_{40} \cdot H_2O$ (99.99% Sigma Aldrich). These solutions were mixed in equal parts, and the 10 μL droplet of this mixture was dropcast onto the cleaned substrate, which were then placed on a hot plate at 120°C until the droplet dried. The Si/SiO_2 substrate was first cleaned with argon gas, and then in an O_2 plasma chamber for 10 min. Before loading the substrate with the deposited metal precursor, the CVD furnace was heated to 500°C under argon flow ($\zeta = 200$ sccm). When the substrate was loaded, the furnace temperature was raised to the growth temperature of 850°C. The sulfur temperature was set to 140°C, and argon flow to 100 sccm. When both temperatures reached their target value, the argon flow was decreased to 75 sccm and the synthesis process was started. After 5 min, the furnace was then quickly cooled to 775°C using compressed air with the argon flow set to 50 sccm, whereas the sample remained in the furnace. Then, the argon flow was stopped ($\zeta = 0$ sccm), the furnace further cooled to 500°C, and the sample was completely removed from the CVD furnace.

Transfer

MoS_2 and WS_2 were moved from the Si wafer by using polydimethylsiloxane (PDMS) transfer (Niehues et al., 2018). The first step is a pickup, in which 2DMs are moved from the growth substrate on the PDMS sheet. In this step, the PDMS sheet (160 μm thick) purchased from GEL-PAK company was cut into a rectangle slightly larger than the Si/SiO_2 substrate and positioned on top of the Si/SiO_2 surface with 2DMs. To increase the separation speed in the following phase, PDMS is left without contact on one of the edges of the Si/SiO_2 substrate, which was ensured by placing a carbon fiber or any similar object on the substrate edge before placing PDMS on top. Subsequently, the PDMS/2DM/substrate is placed on top of a DI (deionized) water and ammonia solution (1,000:1 ratio), which is gently stirred to ensure the flow of the solution. The solution slowly intercalates between the PDMS and Si/SiO_2 substrate, separating 2DM from the Si/SiO_2 substrate. After complete separation in a few minutes, the Si/SiO_2 substrate sinks into the solution, and PDMS with 2DM are left floating on top of the solution. PDMS with 2DM is additionally rinsed with DI water and dried with nitrogen flow to remove residual water from the surface.

For placing 2DMs from PDMS on sapphire, PDMS with 2DM is positioned on top of the sapphire and gently pressed with an Q-tip to ensure adequate adhesion over the whole surface. PDMS with 2DM is fixed on a z-axis manipulator with which the separation of PDMS and sapphire can be controlled. To ensure that the 2DM has higher adhesion with sapphire, PDMS is slowly separated in small steps with a z-axis manipulator. The front of the adhesion is monitored with an optical microscope to increase separation speed in areas of no interest and reduce it in regions with 2DM flakes. After the controlled and complete separation of PMDS, 2DM is left on the sapphire surface. For detailed information about this process, see Castellanos-Gomez et al. (2013).

Sample Preparation

The MoS2 and WS2 substrate monolayers were placed on a microscopic slide and fixed with a coverslip, leaving the layer of air between the two glass surfaces. In addition, we introduced various media with different refractive indices to the monolayers. A small amount of glycerin, with a refractive index of $n = 1.47$ was directly applied on top of the monolayers and then fixed with a coverslip. Distilled water was also used as an embedding medium, but without a coverslip as we employed a "water-dipping" objective lens for this type of samples. During the recording in different embedding media, no degradation of monolayer flakes was observed, so samples prepared in this way can be used several times. This approach allowed us to systematically examine how different embedding media influence resolution assessment.

Objective Lenses

We used a range of objective lenses (see Table 1) to investigate how resolution assessment is affected by different measurement conditions. A variety of different objective lenses was used, taking into account their different NA's, magnifications and using different immersion media. For samples embedded in distilled water, we employed the water-dipping objective lens, specifically W Plan-APOCHROMAT. This type of objective lens is designed to be used without a coverslip, with the tip submerged into the embedding medium.

Theoretical Limit Calculation

The theoretical limits for the lateral and axial resolutions under the different measurement conditions given in this paper were calculated using the following equations (Squier &

Table 1. Overview of Objective Lenses Used (All from Zeiss)

Objective lens	Magnification	Numerical aperture	Immersion	Working distance (mm)	Chromatic aberration correction	Spherical aberration correction
EC Plan-NEOFLUAR	40×	1.30	Oil	0.21	Red and blue; green close	Blue, green
W Plan-APOCHROMAT	40×	1.00	Water-dipping	2.50	Deep blue, blue, green and red	Deep blue and blue
Plan-APOCHROMAT	20×	0.80	—	0.55	Deep blue, blue, green and red	Deep blue and blue
GF Planachromat	40×	0.65	—	0.53	Red and blue	Green

Müller, 2001; van den Bos & den Dekker, 2001; Masters & So, 2009; Farahi, 2015):

$$\mathrm{FWHM}_{\mathrm{lat}} = \frac{1}{\sqrt{N}} \frac{0.51 \cdot \lambda}{\mathrm{NA}} \quad (1)$$

$$\mathrm{FWHM}_{\mathrm{ax}} = \frac{1}{\sqrt{N}} \frac{1.77 \cdot n \cdot \lambda}{\mathrm{NA}^2} \quad (2)$$

with λ representing excitation wavelength, n is the index of refraction of respective embedding media, and N is the nonlinearity order ($N = 2$ for TPEF and SHG, $N = 3$ for THG). We should emphasize that the magnitude for NAs used in all calculation throughout the paper were from the specifications of the objective lenses given by the manufacturer. This can be considered as the best possible approximation as the exact magnitude is only valid under certain conditions (refractive index of the sample/embedding medium and proximity to the coverslip surface) and may vary with different settings/conditions. In other words, if the embedding medium is changed, the refractive index changes and so does the NA which depends on the refractive index. This change cannot be measured or estimated, so the value from the objective specification is used in the calculations for all settings/conditions.

Results

Lateral Resolution in TPEF Modality

WS_2 and MoS_2 monolayers can generate photoluminescence when excited in the 520–640 nm and 610–670 nm ranges (Rigosi et al., 2015). Therefore, they can be used for resolution assessment of fluorescence microscopy modalities in general. However, due to the spectral range of our lasers, it was not possible to obtain a TPEF signal from these monolayers. Therefore, we opted to use 0.2 μm fluorescent spheres to access lateral resolution. The inset in Figure 1 shows the fluorescent spheres recorded in the TPEF modality using the 40 × 1.3 objective lens. By fitting the extracted intensity profile using a Gaussian function, we determined the lateral resolution to be (320 ± 20) nm. The data points for fitting were chosen to include the feature of interest (i.e., peak), while expanding the range did not affect the fitting parameters. The result corresponds to the FWHM of the obtained intensity distribution, with the error representing the fitting error. The lateral resolution in the TPEF modality was only successfully determined at an excitation wavelength of 730 nm. The theoretical limit for lateral resolution in the TPEF modality, which was calculated under the same conditions according to the equation (1), is 203 nm. Excitation at higher wavelengths resulted in insufficient SNR for the resolution measurement. It was not possible to record a stacked image of satisfactory quality for axial resolution assessment due to pronounced photobleaching. It is also important to note that the fluorescent spheres used in this case cannot be considered as point-like sources due to their size and expected resolution. In contrast, the use of TMD monolayers does not lead to photobleaching and eliminates the need for deconvolution due to their subnanometer thickness. Consequently, the application of knife-edge technique to TMD monolayers provides a reliable measurement of both lateral and axial resolution.

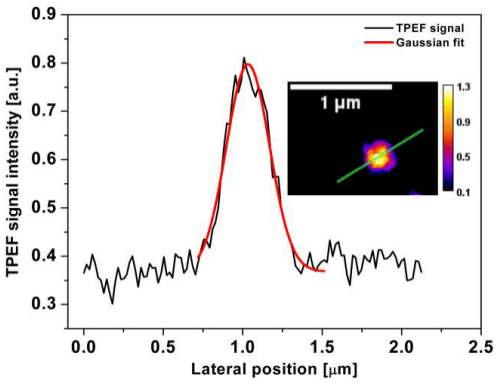

Fig. 1. TPEF signal of a fluorescent bead with a nominal size of 0.2 μm. The individual intensity profile was extracted from the labeled position on the inset. The profile was fitted using a Gaussian function with a quality indicator for the fit of $R^2 = 97.5\%$. The sample was recorded using a 40 × 1.3 objective lens at the excitation wavelength of 730 nm.

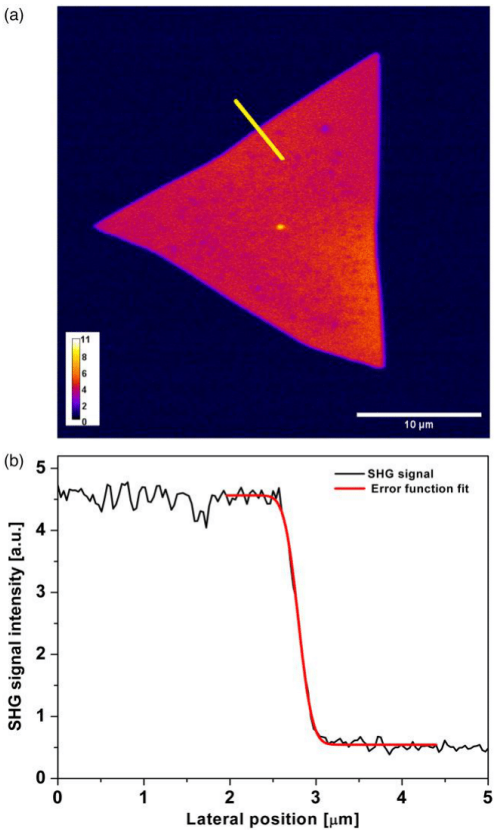

Fig. 2. (**a**) SHG image of a MoS_2 flake. The image was recorded at an excitation wavelength of 800 nm using a 40 × 1.3 objective lens with glycerin as the embedding medium. The marker (line) indicates the position along the edge of the monolayer flake from which the intensity profile was extracted. (**b**) Typical intensity profile extracted at the edge of the MoS_2 monolayer flake. The profile was fitted using the error function, with the parameter for the quality of fit $R^2 = 99.8\%$.

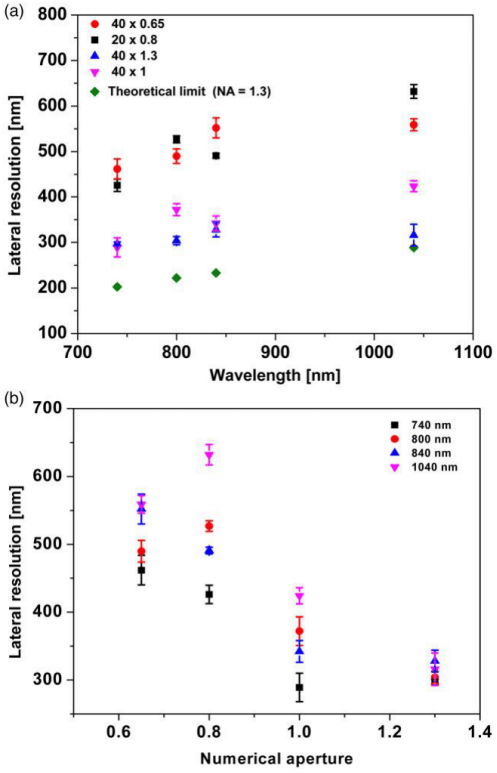

Fig. 3. Dependence of the lateral resolution on (**a**) the excitation wavelength for various objective lenses and (**b**) the numerical aperture for various excitation wavelengths. The results were obtained for a MoS_2 monolayer in the SHG modality.

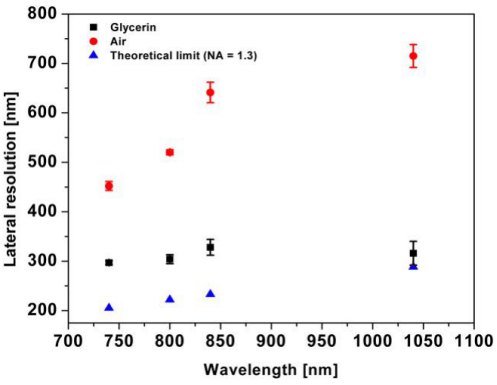

Fig. 4. Dependence of the lateral resolution on the excitation wave length for two embedding media, air, and glycerin. The graph shows the results obtained with a 40 × 1.3 objective lens and the theoretical limit for the lateral resolution under the same measurement conditions. The results were obtained for a MoS_2 monolayer in the SHG modality.

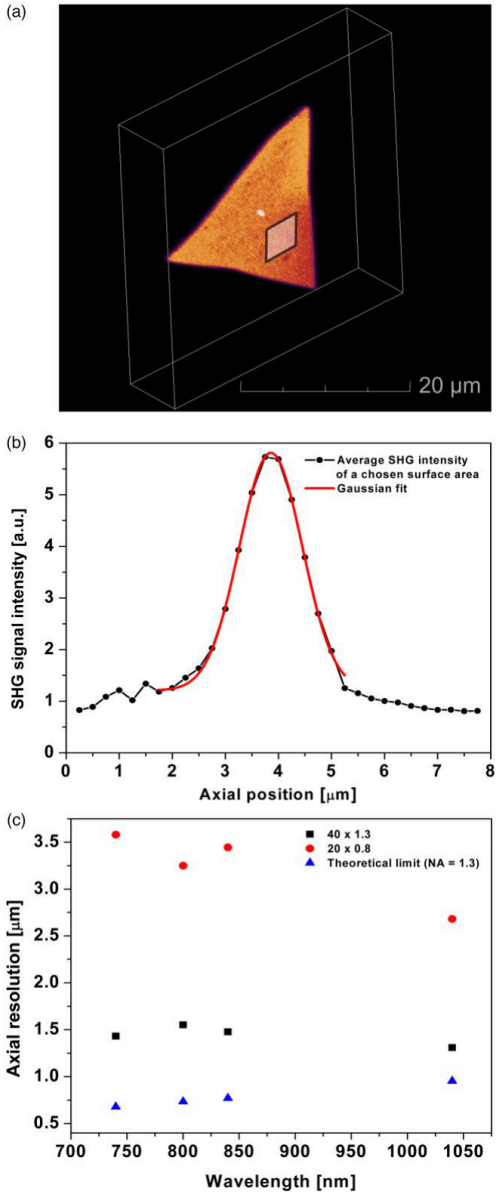

Fig. 5. (**a**) Calibrated 3D model of the MoS_2 monolayer flake with labeled surface from which the average intensity was calculated. (**b**) Intensity profile obtained by averaging the intensity of a chosen surface area of 100 × 100 pixels for each image of the flake in the stack. The *x*-axis represents the axial position of the image plane. The fitting was performed using Gaussian fit, with the quality parameter $R^2 = 99.7\%$. (**c**) Dependence of the axial resolution on the excitation wavelengths in the SHG modality for 40 × 1.3 and 20 × 0.8 objective lenses.

Resolution Assessment in SHG Modality

MoS_2 and WS_2 monolayers were used for resolution measurement in the SHG modality. No significant differences in the resolution assessment were found between these two materials. The typical image of a monolayer flake is shown in Figure 2a. These flakes exhibit distinct and well-defined edges, suitable for lateral resolution assessment using the knife-edge technique. To determine lateral resolution, we extracted intensity profiles over the edge and performed fits using the error function (which is the integral of the Gaussian function) (Davis & Brown, 2002), as shown in Figure 2b. The data points for the fit were chosen to include features of interest (the slope), while further expansion of the range did not affect the fit parameters. The intensity profiles of the monolayer-substrate boundary were analyzed at typically ten different positions along the edge, resulting in a total of 800 processed profiles. The lateral resolution was then calculated based on the mean value of the parameter w (the half-width at $\frac{1}{e^2}$ of the corresponding Gaussian distribution) obtained for each processed monolayer flake, with the error corresponding to the standard error of the mean. The resolution is presented as FWHM of the Gaussian distribution corresponding to the data obtained, where FWHM is calculated as $w/0.85$.

The axial resolution was determined based on the recorded stack, a series of consecutive images taken in equidistant sample planes, of a thin monolayer. A homogeneous surface of approximately 100 × 100 pixels was selected within the monolayer. The same surface was analyzed on all images of the stack. The average value of the pixel intensity of the observed surface was determined. The dependence of the average intensity of the chosen surface area on the corresponding axial position of the image plane was fitted by the Gaussian function. The FWHM parameter of the Gaussian fit was read directly as the axial resolution of the microscope under the specified conditions, with the error corresponding to the fitting error.

Both lateral and axial resolutions were presented as the FWHM values, all in accordance with the Houston criterion for resolution. An identical data analysis procedure was applied for resolution assessment in THG modality.

Table 2. Comparison of Axial Resolutions in SHG Modality between Different Embedding Media and Objective Lenses, along with the Theoretical Limits Provided in Brackets.

SHG	740 nm	800 nm
Glycerin	1.4 μm (0.81 μm)	1.6 μm (0.87 μm)
Air	5.9 μm (0.55 μm)	6.7 μm (0.59 μm)

The theoretical limits were calculated using the equations (1) and (2) with the refractive indices of glycerin and air: $n = 1.47$ and $n = 1$, respectively.

Lateral Resolution in SHG Modality

To investigate wavelength-dependent variation in lateral resolution of the microscope, we recorded SHG signal of the monolayer flake at four different excitation wavelengths: 740 nm, 800 nm, 840 nm, and 1,040 nm, using glycerin as the embedding medium. The dependence of the resolution on wavelength for different NA's of objective lenses is shown in Figure 3a. The graph illustrates the theoretical limit of lateral resolution for the objective lens with a numerical aperture of 1.3 at different wavelengths. The experimental results align with expectations and show a deterioration of resolution with increasing wavelength for the specific objective lens. A lower value indicates better resolution and vice versa. An exception was noted at 800 nm, where better resolution was achieved with a lower NA objective lens (0.8 versus 0.65). A similar apparent exception was also observed at 740 nm (1.0 versus 1.3), which is within the experimental margin of error. Additionally, the obtained values are above the theoretical limit at all wavelengths. Figure 3b shows the dependence of the lateral resolution on the NA of the corresponding objective lenses for different wavelengths. The results are generally in line with expectations, with two exceptions observed for objective lenses with NA values of 0.8 and 1.0, where better resolution was achieved at 840 nm compared to 800 nm. The aforementioned exceptions might be attributed to the fact that the objective lenses used in this study are not designed for infrared light but for visible light (see Table 1), resulting in suboptimal focusing. This may vary from case to case (for different objectives, at different wavelengths). The lateral resolution for the 40 × 1.3 objective lens exhibits weak wavelength dependence, which agrees well with the theoretical limit shown in Figure 3a. As the monolayer flakes are significantly thinner than the expected resolution, deconvolution is not required. Notably, no photobleaching of the samples was observed at any wavelength during monolayer imaging.

In addition to the factors already mentioned, resolution is further influenced by the order of interaction. While TPEF

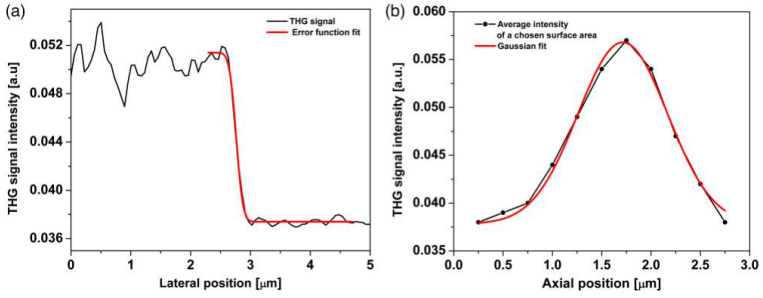

Fig. 6. (**a**) Typical intensity profile extracted at the edge of the WS_2 monolayer flake in THG modality for a 40 × 1.3 objective lens. The profile was fitted using the error function, with the quality of fit parameter $R^2 = 99.6\%$. (**b**) Intensity distribution obtained by averaging the intensity of a chosen area of 60 × 60 pixels for each image in the stack. The *x*-axis represents the axial position of the image plane. Fitting was performed using the Gaussian function, with the quality parameter of fit $R^2 = 99\%$.

and SHG are conceptually distinct processes, both involve two-photon interactions, suggesting that the resolutions obtained for the corresponding imaging modalities should be closely aligned. This implies that the theoretical limit will be the same for both imaging modalities at a given wavelength. Despite the slightly higher excitation wavelength of 740 nm used for the resolution measurement in the SHG modality, the measured resolution of (300±10) nm exceeds that of the TPEF modality (320±20) nm obtained at 730 nm. However, this statement is not conclusive as the measurements are within the margin of error. Both measurements were performed using a 40 × 1.3 objective lens. The fluorescent beads utilized in our study do not serve as ideal point-like sources for resolution measurement. In contrast, monolayer flakes due to their extensive thinness, offer a better approximation when combined with the knife-edge technique.

Using the same method, we also investigated the influence of the embedding medium on the lateral resolution of the SHG modality. We recorded images of monolayer flakes at various excitation wavelengths using a 40 × 1.3 objective lens, with one sample embedded in glycerin and the other in air. Figure 4 illustrates the lateral resolution for the two specified embedding media. It is shown that the resolution is closer to the theoretical limit when glycerin is present at all excitation wavelengths used, indicating a more appropriate utilization of the objective lens.

Axial Resolution in SHG Modality

In addition to assessing lateral resolution, we also investigated axial resolution using the same samples. The SHG signal of glycerin-embedded monolayer flakes was recorded at various excitation wavelengths. For each wavelength, a stack of typically 30 images was acquired, with a slice spacing of 0.25 μm. To determine the axial resolution at a specific wavelength, we selected a homogeneous surface area from each image of the stack. Figure 5a displays the calibrated 3D model of the monolayer flake and provides an example of the surface used to derive parameters for axial resolution assessment. The resolution was determined based on the dependence of average intensity of the chosen surface area on the corresponding axial position of the image plane in the stack. This is shown in Figure 5b. This dependence was fitted with a Gaussian function and the FWHM was determined as a measure of resolution. The measurement involved two objective lenses with distinct NA values with an aim to investigate how the resolution varies with the NA for different wavelengths. The corresponding results are shown in Figure 5c together with the theoretical resolution limit in the case of an objective lens with an NA value of 1.3. Although the obtained resolution is above the theoretical limit, the observed trend deviates from expectations and indicates an improvement in resolution with increasing wavelength, which is particularly evident for the 20 × 0.8 objective lens. A similar trend can be seen for the 40 × 1.3 objective lens. As expected, superior results were consistently obtained with the higher NA objective lens.

We also investigated how axial resolution is affected by the embedding medium. The SHG signal of MoS_2 monolayer flakes was recorded using a 40 × 1.3 objective lens at excitation wavelengths of 740 nm and 800 nm, using glycerin and air as embedding media. A comparison between the axial resolutions obtained for different embedding media is provided in Table 2. Significantly poorer results were obtained when air was used as the embedding medium.

Table 3. Comparison of Lateral and Axial Resolution in THG Modality between Different Embedding Media and Objective Lenses, along with the Theoretical Limits Provided in Brackets.

THG (1,040 nm)	Lateral Resolution (μm)		Axial Resolution (μm)
	20 × 0.8	40 × 1.3	40 × 1.3
Glycerin	0.44 (0.39)	0.27 (0.24)	1.10 (0.92)
Air	0.75 (0.39)	0.43 (0.24)	5.90 (0.63)

The theoretical limits were calculated using the equations (1) and (2) with the refractive indices of glycerin and air: $n = 1.47$ and $n = 1$, respectively.

Resolution Assessment in THG Modality

We measured both lateral and axial resolution of the microscope in the THG modality using WS_2 monolayer flakes immersed in glycerin with an excitation wavelength of 1,040 nm and a 40 × 1.3 objective lens. Figure 6a shows a typical intensity profile extracted from the edge of the monolayer flake. This profile was fitted with the error function, resulting in a lateral resolution of (270 ± 10) nm. Figure 6b shows the distribution of the average intensities of the selected surface area from each image of the stack (slice separation of 0.25 μm) over the axial position of the image plane. Using this profile, we were able to determine the axial resolution to be (1.07 ± 0.06) μm. We investigated how both the lateral and axial resolution in THG modality vary between different embedding media and objective lenses. An overview of the results is displayed in Table 3, which quantifies the effect of embedding media with different refractive indices on image

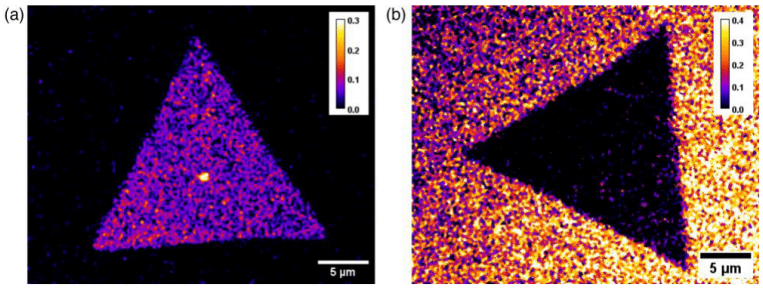

Fig. 7. (**a**) MoS_2 monolayer flake with glycerin as the embedding medium. (**b**) MoS_2 monolayer flake with air as embedding medium. The figure clearly shows decreasing of the THG signal in air.

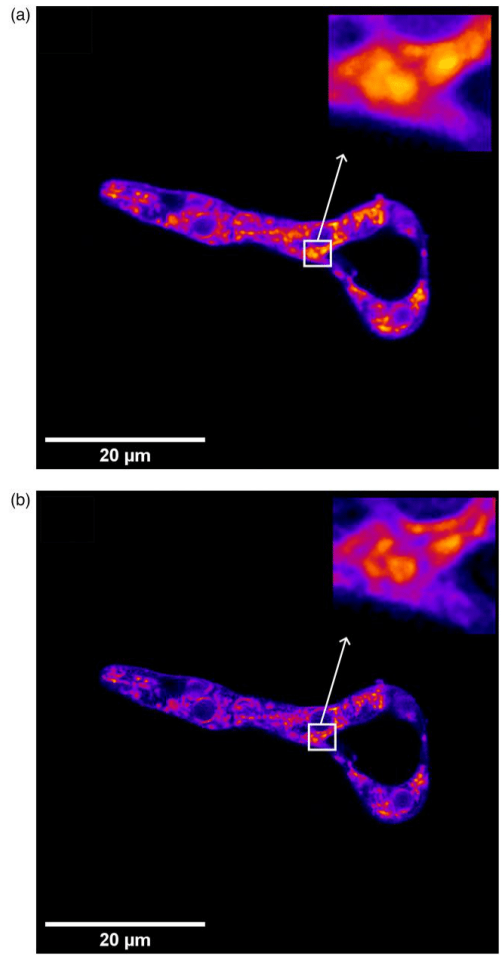

Fig. 8. TPEF signal of *Phycomyces blakesleeanus* hyphae, stained with the vital mitochondrial dye Rhodamine123, excitation wavelength 800 nm, laser power 2 mW, emission filters: VIS (400–700 nm) bandpass filter (from EOS50D camera, Canon), and 530/43 bandpass filter (MF530-43, Thorlabs, Inc.). (**a**) Original, unprocessed image. (**b**) Image deconvoluted using the Richardson–Lucy algorithm in MATLAB software. Deconvolution was performed using the Gaussian distribution with a FWHM equivalent to the FWHM of the PSF measured under identical experimental conditions. The insets show that smaller mitochondria can be resolved when the image is deconvoluted.

resolution. Here, too, significantly poorer results were achieved for the resolution in air.

An interesting observation is that the THG signal of MoS_2 monolayer flakes in glycerin differs from that in air. More specifically, the MoS_2 monolayer flake exhibits a dominant THG signal in glycerin over the substrate-glycerin interface, whereas the same monolayer flake in air suppresses the THG signal. Figure 7a shows the THG signal of MoS_2 immersed in glycerin is presented, whereas Figure 7b demonstrates how the THG signal from the sapphire substrate dominates over the THG signal of the MoS_2 monolayer flake. It is known from the literature that the $\chi^{(3)}$ values of 2DMs depend on the excitation wavelengths (Autere et al., 2018, and references therein; Wang et al., 2013) as well as other parameters such as strain, defects, doping, substrates, and chemical treatment (Autere et al., 2018, and references therein). Here, the only difference between these two systems is the interface, which causes the increase in the nonlinear optical response through phenomenological surface-enhanced THG discussed in Tsang (1995). Although a detailed explanation of this effect is beyond the scope of this discussion, it is worth noting that even in this case, an inverted edge emerges that allows resolution assessment using the knife-edge technique. There is no difference in the assessment of SHG resolution when either material is used.

Image Resolution Improvement by Deconvolution

The PSF full-width values presented in this paper can be used as input data for deconvolution to improve the resolution of images acquired with this NLSM setup. Deconvolution is particularly important for improving image quality when dealing with samples containing structures whose dimensions are very close to the resolution limit, as it enables them to be visualized as distinct and separate objects. Figure 8 shows a representative image before (a) and after (b) deconvolution, highlighting a significant improvement in the efficiency of discerning and identifying small objects within the sample. In Figure 8, the image was deconvoluted using the Richardson–Lucy algorithm in MATLAB software. The deconvolution was performed using a Gaussian distribution with a FWHM equivalent to the FWHM of PSF measured under identical experimental conditions.

Conclusion

We have presented measurements of resolution for all imaging modalities (TPEF, SHG, and THG) of our custom-built NLSM using two distinct approaches. We performed a direct assessment of both lateral (using fluorescent nanospheres in the TPEF modality) and axial resolution (in the SHG and THG modalities). The assessment of lateral resolution in the SHG and THG modalities was performed using the knife-edge technique on WS_2 and MoS_2 monolayers. The lateral technique offers a higher SNR, no photobleaching effect and shows good agreement with the conventional resolution measurement technique using fluorescent nanospheres. Assessing SHG and THG imaging resolution by the knife-edge method overcomes the coherence problem encountered when probing with small (point-like) objects. The obtained results, namely the PSF FWHM values, were employed in image processing by deconvolution, for resolution enhancement.

In addition, we performed a comprehensive analysis of how the resolution varies with numerical aperture of the objective lens, excitation wavelength and refractive index of the embedding medium. The results closest to the theoretical limit were obtained when glycerin was used as the embedding medium at all wavelengths, for both SHG and THG imaging modalities and all objective lenses examined. The latter implies that various embedding media can significantly influence resolution and thus the quality of acquired images. The use of a suitable medium might lead to significantly better imaging results, as objective lenses are usually designed for biological samples embedded in media with a refractive index above 1. As a side note, the intensity of the THG signal from TMD

monolayers strongly depends on the substrate- monolayer-medium combination and can either be enhanced or suppressed. For example, MoS_2 monolayer flakes show a pronounced THG signal in glycerin over the substrate-glycerin interface, while the same monolayer flakes in air suppress the THG signal.

In conclusion, the proposed use of WS_2 and MoS_2 monolayers has emerged as a promising tool for the characterization not only of nonlinear imaging systems in terms of lateral and axial resolution, but also of various microscopic systems.

Availability of Data and Materials

The authors have declared that no datasets apply for this piece.

Acknowledgments

We would like to thank Milan Minić for indispensable technical help and support. We thank Professor Michael Pravica from University of Nevada, Las Vegas (UNLV) for reviewing the manuscript.

Author Contributions Statement

J.Z.J. drafted the manuscript, processed the data and reviewed the literature, M.B. performed the measurements, processed the data and reviewed the literature, A.D. sorted out and processed the data and reviewed the literature, A.S. synthesized the MoS_2 monolayer flakes, L.Ž. synthesized the WS_2 monolayer flakes, B.R. performed the PDMS transfer, N.V. supervised the synthesis, T.P. grown the fungi and prepare the sample, M.D.R and A.J.K. built the instrument, performed measurements, processed the data, conceptualized and supervised the research. All authors reviewed the manuscript. J.Z.J., M.B., and A.D. contributed equally to this work. This paper will be the part of midterm check point in their PhD studies.

Financial Support

This research was supported by the Science Fund of the Republic of Serbia, Grant No. 4545, project "Advanced Biophysical Methods for Soil Targeted Fungi-Based Biocontrol Agents" - BioPhysFUN; and the Institute of Physics Belgrade, through the grant by the Ministry of Science, Technological Development and Innovations of the Republic of Serbia. A.S., B.R., and N.V. acknowledge the support of Croatian Science Foundation, Grant No. UIP-2017-05-3869, Centre of Excellence for Advanced Materials and Sensing Devices, ERDF Grant No. KK.01.1.1.01.0001 and Centre for Advanced Laser Techniques, ERDF Grant KK.01.1.1.05.

Conflict of Interest

The authors declare that they have no competing interest.

References

Araújo M, Silva R, Lima E, Pereira D & De Oliveira P (2009). Measurement of Gaussian laser beam radius using the knife-edge technique: Improvement on data analysis. *Appl Opt* **48**, 393–396. https://doi.org/10.1364/AO.48.000393

Autere A, Jussila H, Dai Y, Wang Y, Lipsanen H & Sun Z (2018). Nonlinear optics with 2D layered materials. *Adv Mater* **30**(24), e1705963. https://doi.org/10.1002/adma.201705963

Castellanos-Gomez A, Buscema M, Zant H & Steele G (2013). Deterministic transfer of two-dimensional materials by all-dry viscoelastic stamping. *2D Mater* **1**, 011002. https://doi.org/10.1088/2053-1583/1/1/011002

Chen X, Nadiarynkh O, Plotnikov S & Campagnola P (2012). Second harmonic generation microscopy for quantitative analysis of collagen fibrillar structure. *Nat Protoc* **7**(4), 654–669. https://doi.org/10.1038/nprot.2012.009

Chu S-W, Tai S-P, Ho C-L, Lin C-H & Sun C-K (2005). High-resolution simultaneous three-photon fluorescence and third-harmonic-generation microscopy. *Microsc Res Tech* **66**(4), 193–197. https://doi.org/10.1002/(ISSN)1097-0029

Cole R, Jinadasa T & Brown C (2011). Measuring and interpreting point spread functions to determine confocal microscope resolution and ensure quality control. *Nat Protoc* **6**(12), 1929–1941. https://doi.org/10.1038/nprot.2011.407

Davis B & Brown G (2002). Diffraction by a randomly rough knife edge. *IEEE Trans Antenn Propag* **50**(12), 1769–1778. https://doi.org/10.1109/TAP.2002.804019

Farahi N. (2015). Resolution analysis of films with embedded spheres for imaging of nanoplasmonic arrays. Thesis. ProQuest LLC, Ann Arbor, MI. Available at https://www.proquest.com/openview/bea17cff0074a8c98f01910ec4d90533/1?pq-origsite=gscholar&cbl=18750

Hou R & Labarthet F (2018). Second harmonic generation microscopy from non-centrosymmetric gold half-coated polystyrene spheres. *Surf Sci* **676**, 46–50. https://doi.org/10.1016/j.susc.2018.01.014

Kozubek M (2001). Theoretical versus experimental resolution in optical microscopy. *Microsc Res Tech* **53**(2), 157–166. https://doi.org/10.1002/jemt.1080

Kumar N, Najmaei S, Cui Q, Ceballos F, Ajayan P, Lou J & Zhao H (2013). Second harmonic microscopy of monolayer MoS_2. *Phys Rev B* **87**(16), 161403. https://doi.org/10.1103/PhysRevB.87.161403

Lee G, Jyothsna K, Park J, Lee J, Raghunathan V & Kim H (2023). Confocal nonlinear optical imaging on hexagonal boron nitride nanosheets. *PhotoniX* **4**(1), 27. https://doi.org/10.1186/s43074-023-00103-6

Li Y, Rao Y, Mak K, You Y, Wang S, Dean C & Heinz T (2013). Probing symmetry properties of few-layer MoS_2 and h-BN by optical second-harmonic generation. *Nano Lett* **13**(7), 3329–3333. https://doi.org/10.1021/nl401561r

Mahou P, Malkinson G, Chaudan É., Gacoin T, Beaurepaire E & Supatto W (2017). Metrology of multiphoton microscopes using second harmonic generation nanoprobes. *Small* **13**, 1701442. https://doi.org/10.1002/smll.201701442

Masihzadeh O, Schlup P & Bartels R (2009). Enhanced spatial resolution in third-harmonic microscopy through polarization switching. *Opt Lett* **34**, 1240–1242. https://doi.org/10.1364/OL.34.001240

Masters B & So P (2009). Handbook of biomedical nonlinear optical microscopy. *J Biomed Opt* **14**, 019901. https://doi.org/10.1117/1.3077566

Mehravar S, Cromey B & Kieu K (2020). Characterization of multiphoton microscopes by nonlinear knife-edge technique. *Appl Opt* **59**(22), G219–G224. https://doi.org/10.1364/AO.391881

Mennel L, Furchi MM, Wachter S, Paur M, Polyushkin DK & Mueller T (2018). Optical imaging of strain in two-dimensional crystals. *Nat Commun* **9**(1), 516. https://doi.org/10.1038/s41467-018-02830-y

Mylonakis M, Tserevelakis G, Vlachos G, Fanouraki E, Pavlopoulos A, Pavlidis M & Zacharakis G (2024). Bimodal optical and optoacoustic multiview microscope in the frequency-domain. *Opt Lett* **49**(3), 462–465. https://doi.org/10.1364/OL.510384

Niehues I, Blob A, Stiehm T, Schmidt R, Jadriško V, Radatović B, Čapeta D, Kralj M, Michaelis de Vasconcellos S & Bratschitsch R (2018). Strain transfer across grain boundaries in MoS_2 monolayers grown

by chemical vapor deposition. *2D Mater* **5**(3), 031003. https://doi.org/10.1088/2053-1583/aaba9a

Pajić T, Todorovic N, Živić M, Nikolic S, Rabasović M, Clayton A & Krmpot A (2022). Label-free third harmonic generation imaging and quantification of lipid droplets in live filamentous fungi. *Sci Rep* **12**(1), 18760. https://doi.org/10.1038/s41598-022-23502-4

Rabasovic M, Pantelic D, Jelenkovic B, Ćurčić S, Rabasovic M, Vrbica M, Lazovic V, Curcic B & Krmpot A (2015). Nonlinear microscopy of chitin and chitinous structures: A case study of two cave-dwelling insects. *J Biomed Opt* **20**(1), 016010–016010. https://doi.org/10.1117/1.JBO.20.1.016010

Radisavljevic B, Radenovic A, Brivio J, Giacometti V & Kis A (2011). Single-layer MoS_2 transistors. *Nat Nanotechnol* **6**, 147–150. https://doi.org/10.1038/nnano.2010.279

Rigosi AF, Hill HM, Li Y, Chernikov A & Heinz TF (2015). Probing interlayer interactions in transition metal dichalcogenide heterostructures by optical spectroscopy: MoS_2/WS_2 and $MoSe_2/WSe_2$. *Nano Lett* **15**(8), 5033–5038. https://doi.org/10.1021/acs.nanolett.5b01055

Rohrbacher A, Olarte OE, Villamaina V, Loza-Alvarez P & Resan B (2017). Multiphoton imaging with blue-diode-pumped SESAM-modelocked Ti:sapphire oscillator generating 5 nJ 82 fs pulses. *Opt Express* **25**(9), 10677–10684. https://doi.org/10.1364/OE.25.010677

Rosa H, Wei H, Verzhbitskiy I, Rodrigues M, Taniguchi T, Watanabe K, Eda G, Pereira V & Gomes J (2018). Characterization of the second- and third-harmonic optical susceptibilities of atomically thin tungsten diselenide. *Sci Rep* **8**(1), 10035. https://doi.org/10.1038/s41598-018-28374-1

Senkić A, Bajo J, Supina A, Radatović B & Vujičić N (2023). Effects of CVD growth parameters on global and local optical properties of MoS2 monolayers. *Mater Chem Phys* **296**, 127185. https://doi.org/10.1016/j.matchemphys.2022.127185

Squier J & Müller M (2001). High resolution nonlinear microscopy: A review of sources and methods for achieving optimal imaging. *Rev Sci Instrum* **72**(7), 2855–2867. https://doi.org/10.1063/1.1379598

Tsang TY (1995). Optical third-harmonic generation at interfaces. *Phys Rev A* **52**(5), 4116–4125. https://doi.org/10.1103/PhysRevA.52.4116

Tserevelakis G, George F, Krmpot A, Vlachos M, Fotakis C & Tavernarakis N (2010). Imaging *Caenorhabditis elegans* embryogenesis by third-harmonic generation microscopy. *Micron* **41**, 444–447. https://doi.org/10.1016/j.micron.2010.02.006

Tserevelakis G, Psycharakis S, Resan B, Brunner F, Gavgiotakis E, Weingarten K & George F (2012). Femtosecond laser nanosurgery of sub-cellular structures in HeLa cells by employing Third Harmonic Generation imaging modality as diagnostic tool. *J Biophotonics* **5**, 200–207. https://doi.org/10.1002/jbio.201100055

van den Bos A & den Dekker A (2001). Resolution reconsidered-conventional approaches and an alternative. In *Advances in Imaging and Electron Physics*, Peter H (Ed.), vol. **117**, pp. 241–360. Amsterdam: Elsevier.

Wachulak PW, Torrisi A, Bartnik A, Wegrzyński Ł, Fok T & Fiedorowicz H (2017). A desktop extreme ultraviolet microscope based on a compact laser-plasma light source. *Appl Phys B* 123, 1–5. https://doi.org/10.1007/s00340-016-6595-5

Wang R, Chien H-C, Kumar J, Kumar N, Chiu H-Y & Zhao H (2013). Third-harmonic generation in ultrathin films of MoS_2. *ACS Appl Mater Interfaces* **6**(1), 314–318. https://doi.org/10.1021/am4042542

Woodward R, Murray R, Phelan C, Oliveira R, Runcorn T, Kelleher E, Li S, de Oliveira E, Fechine GJM, Eda G & de Matos C (2016). Characterization of the second- and third-order nonlinear optical susceptibilities of monolayer MoS_2 using multiphoton microscopy. *2D Mater* **4**(1), 011006. https://doi.org/10.1088/2053-1583/4/1/011006

Yin X, Ye Z, Chenet D, Ye Y, O'Brien K, Hone J & Zhang X (2014). Edge nonlinear optics on a MoS_2 atomic monolayer. *Science* **344**(6183), 488–490. https://doi.org/10.1126/science.1250564

Zipfel W, Williams R & Webb W (2003). Nonlinear magic: Multiphoton microscopy in the biosciences. *Nat Biotechnol* **21**(11), 1369–1377. https://doi.org/10.1038/nbt899

photonics

MDPI

Article

Improving the Two-Color Temperature Sensing Using Machine Learning Approach: $GdVO_4:Sm^{3+}$ Prepared by Solution Combustion Synthesis (SCS)

Jovana Z. Jelic [1], Aleksa Dencevski [1], Mihailo D. Rabasovic [1], Janez Krizan [2], Svetlana Savic-Sevic [1], Marko G. Nikolic [1], Myriam H. Aguirre [3,4,5], Dragutin Sevic [1,*] and Maja S. Rabasovic [1,*]

[1] Institute of Physics, University of Belgrade, Pregrevica 118, 11080 Belgrade, Serbia; jelic@ipb.ac.rs (J.Z.J.); dencevski@ipb.ac.rs (A.D.); rabasovic@ipb.ac.rs (M.D.R.); savic@ipb.ac.rs (S.S.-S.); nikolic@ipb.ac.rs (M.G.N.)
[2] AMI, d.o.o, 2250 Ptuj, Slovenia; janez.krizan@gmail.com
[3] Department of Condensed Matter Physics, University of Zaragoza, E-50009 Zaragoza, Spain; maguirre@unizar.es
[4] Instituto de Nanociencia y Materiales de Aragón, University of Zaragoza-CSIC, E-50018 Zaragoza, Spain
[5] Laboratorio de Microscopías Avanzadas, Universisity of Zaragoza, E-50018 Zaragoza, Spain
* Correspondence: sevic@ipb.ac.rs (D.S.); majap@ipb.ac.rs (M.S.R.)

Abstract: The gadolinium vanadate doped with samarium ($GdVO_4:Sm^{3+}$) nanopowder was prepared by the solution combustion synthesis (SCS) method. After synthesis, in order to achieve full crystallinity, the material was annealed in air atmosphere at 900 °C. Phase identification in the post-annealed powder samples was performed by X-ray diffraction, and morphology was investigated by high-resolution scanning electron microscope (SEM) and transmission electron microscope (TEM). Photoluminescence characterization of emission spectrum and time resolved analysis was performed using tunable laser optical parametric oscillator excitation and streak camera. In addition to samarium emission bands, a weak broad luminescence emission band of host VO_4^{3-} was also observed by the detection system. In our earlier work, we analyzed the possibility of using the host luminescence for two-color temperature sensing, improving the method by introducing the temporal dependence in line intensity ratio measurements. Here, we showed that further improvements are possible by using the machine learning approach. To facilitate the initial data assessment, we incorporated Principal Component Analysis (PCA), t-Distributed Stochastic Neighbor Embedding (t-SNE) and Uniform Manifold Approximation and Projection (UMAP) clustering of GdVO4:Sm^{3+} spectra at various temperatures. Good predictions of temperature were obtained using deep neural networks. Performance of the deep learning network was enhanced by data augmentation technique.

Keywords: samarium-doped gadolinium vanadate nanopowder; structural and luminescent properties; lifetime; phosphor thermometry; machine learning

Citation: Jelic, J.Z.; Dencevski, A.; Rabasovic, M.D.; Krizan, J.; Savic-Sevic, S.; Nikolic, M.G.; Aguirre, M.H.; Sevic, D.; Rabasovic, M.S. Improving the Two-Color Temperature Sensing Using Machine Learning Approach: $GdVO_4:Sm^{3+}$ Prepared by Solution Combustion Synthesis (SCS). *Photonics* **2024**, *11*, 642. https://doi.org/10.3390/photonics11070642

Received: 6 June 2024
Revised: 2 July 2024
Accepted: 3 July 2024
Published: 6 July 2024

1. Introduction

In this paper, we present the results of experimental investigation of Sm^{3+}-doped $GdVO_4$ nanopowders. Nanopowder $GdVO_4$:Sm is an efficient orange-reddish light-emitting material [1]; light emission occurs due to a strong absorption of ultraviolet light by $GdVO_4$ and efficient energy transfer from vanadate groups (VO_4^{3-}) to dopants (Sm^{3+}). It is a good candidate for phosphor thermometry [1,2] Here, it is prepared by the solution combustion synthesis (SCS) method [1]. Simplicity and low cost are the main characteristics of this process. Phase identification in the post-annealed powder samples is performed by X-ray diffraction, and morphology is investigated by high-resolution scanning electron microscope (SEM) and by transmission electron microscopy (TEM). The main aim of this study is time-resolved analysis of luminescence properties of $GdVO_4:Sm^{3+}$ nanopowders. The possibility for $GdVO_4:Sm^{3+}$ usage in phosphor thermometry was analyzed in ref. [2], where

temperature determination of sensing calibration curves was based on luminescence intensity ratios of samarium lines. In ref. [1], we used the intensity ratio of the host luminescence emission and samarium line to obtain temperature-sensing calibration curves, as proposed in refs. [3–6]. Calculation of temperature by intensity ratio of two luminescence peaks of different colors is called two-color thermometry. In ref. [1], the method was improved by introducing temporal dependence in the ratio measurements, as proposed in ref. [7]. Here, we propose a different approach, based on machine learning (ML). ML techniques are more and more used in the analysis of luminescence, near-infrared, and other spectral data [8–18]. Our findings demonstrate that instead of the conventional approach of identifying spectral peaks and calculating intensity ratios, it is feasible to train computer software to recognize time-resolved spectra associated with different temperatures of the thermophosphor. Traditionally, luminescence thermometric methods rely on analyzing a single spectral characteristic parameter, selected based on the properties of the thermophosphor and the researcher's intuition or experience. This approach leads to a partial utilization of spectral data, limiting measurement accuracy and thermal resolution. In contrast, the authors of [12] trained a deep learning artificial neural network to extract multiple temperature-dependent features for temperature estimation, fully utilizing temperature-dependent spectral data. However, the spectral data in ref. [12] did not include temporal information. In our research, we take a step further by incorporating time-resolved spectra into machine learning (ML)-based temperature estimation using a deep learning artificial neural network. This approach allows us incorporation of the thermophosphor's lifetime dependence into our analysis. In ref. [18], our measurements were aimed to be used by ML. We performed 50 measurements for each temperature of the sample. Upon inspecting the measured spectra in ref. [18], we realized that they have very small intensity differences, as expected. The main differences between the spectra acquired at the same temperature were contents of random noise introduced by the photon-counting operation of streak camera. On the other hand, in this study, we analyze measurements which were not obtained specifically for ML; in other words, there was not a large enough training set of training data for ML. To overcome this difficulty. we used the data augmenting techniques; see [19] and references therein.

2. Materials and Methods

$GdVO_4$ nanopowder doped with samarium ions was prepared by the solution combustion method, as described in ref. [1]. Stoichiometric quantities of starting chemicals $Sm(NO_3)_3$, $Gd(NO_3)_3{\cdot}6H_2O$, and NH_4VO_3 with the purity of 99.99% were chosen to obtain the Sm^{3+} concentration in $GdVO_4$ of 1 at.% ($Gd_{1-0.01}Sm_{0.01}VO_4$). All the chemicals and ammonium nitrate NH_4NO_3 were purchased from ABCR, and urea, $(NH_2)_2CO$, from Sigma-Aldrich Merck KGaA, Darmstadt, Germany. The dry mixture of 0.134 g (0.4 mmol) of $Sm(NO_3)_3$, 18.05 g (40 mmol) of $Gd(NO_3)_3{\cdot}6H_2O$, and 4.676 g (40 mmol) of NH_4VO_3 was combined with the mixture of 4.8 g (60 mmol) of ammonium nitrate and 3.003 g (50 mmol) of urea, which were used as organic fuels. The prepared starting reagents were combusted with aflame burner at approximately 500 °C, yielding a voluminous foamy powder in an intensive exothermic reaction. After the solution combustion synthesis, the nanopowder was annealed for 2 h, in air atmosphere, at 900 °C. Annealing has an effect on increasing the grain size of the nanopowders and it is widely used to achieve higher emission intensity.

The structure of the nanopowder was verified by X-ray diffraction analysis using a Diffractometer system: EMPYREAN, PANalytical. X-ray diffraction analysis (XRD) was performed using a X-ray Diffractometer PANalytical Empyrean, Malvern Panalytical, Malvern, United Kingdom with monochromatic CuK α radiation ($\gamma = 0.15405980$) at 45 kV and 40 mA. The diffraction data for the GdVO4-Sm nanopowder were collected over a 2θ range from 5 to 110° at a scan rate of 0.4° per minute.

The morphology of nanopowders and the size of crystallites were determined by a high-resolution scanning electron microscope (SEM) equipped with a high-brightness Schottky Field Emission gun FEGSEM, TESCAN Brno—Kohoutovice Czech Republic.

The morphology of GdVO4-Sm nanopowder was also evaluated by transmission electron microscopy (TEM), FEI Tecnai F30 Hillsboro, Oregon, United States. Photoluminescence (PL) studies reported in this work were performed using the Optical Parametric Oscillator Vibrant OPO Carlsbad, California USA, as described in ref. [1]. The output of the OPO can be continuously tuned over a spectral range from 320 nm to 475 nm. Time-resolved streak images of the emission spectrum excited by the OPO system were collected using a spectrograph (SpectraPro 2300i), Teledyne Princeton Instruments, New Jersey USA and recorded with a Hamamatsu streak camera (model C4334), Hamamatsu City, Japan. All streak camera operations were controlled by HPD-TA 8.3.0 (High-Performance Digital Temporal Analyzer) software. For measurements presented here, we used a homemade temperature control system, similar to the one in ref. [20].

To perform the machine learning (ML) analysis of the data, we utilized the Solo + Mia software package (Version 9.1, Eigenvector Research Inc, Manson, Washington USA). Solo provides a user-friendly environment, making it usable to individuals without programming expertise.

The measured spectra were initially analyzed using Principal Component Analysis (PCA) and Uniform Manifold Approximation and Projection clustering (UMAP). PCA was originally introduced in ref. [21], and for further details, we refer the reader to [22] and the referenced sources therein. Efficient implementation of t-SNE is proposed in ref. [23].

UMAP, a novel clustering technique suitable for visualizing extensive datasets, was recently proposed in ref. [24]. Ultimately, after conducting preliminary visualization experiments, we employed a deep learning artificial neural network to estimate the temperature of the heated samples.

3. Results

3.1. TEM, XRD, and SEM Study

The morphology of $GdVO_4$:Sm nanopowder was evaluated by transmission electron microscopy (TEM). TEM analysis shows the presence of slightly elongated particles formed by much smaller monocrystals as presented in Figure 1a. High-resolution TEM (HRTEM) shown in Figure 1b exposes their good crystallinity, clear lattice fringes, and the interplanar spacing of 4.77 Å, which might be associated with the (101) plane of the tetragonal $GdVO_4$ phase. Selected area electron diffraction (SAED) and fast Fourier transform (FFT) analyses revealed d values of 4.77 Å, 3.61 Å, 2.69 Å, 2.55 Å, and 1.86 Å, which match well with the (101), (200), (112), (220), and (312) crystal planes of the tetragonal $GdVO_4$ phase (JCPDS 00-017-0260). We confirmed the coexistence of a cubic Gd_2O_3 phase, specifically the (222) and (400) planes, with the corresponding d values of 3.11 Å and 2.70 Å (JCPDS 01-073-6280). In addition, the monophase composition of particles was identified by the presence of the above-mentioned crystal planes with d values corresponding well to those obtained through the X-ray diffraction (XRD) analysis of the sample presented in Figure 2.

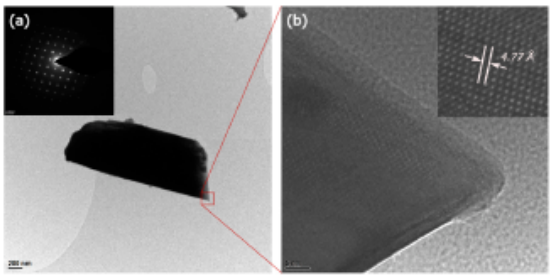

Figure 1. (a) TEM image of $GdVO_4$-Sm nanoparticles with the inset showing the SAED pattern. (b) HRTEM image of a section of the nanoparticle highlighted in the red square in (a). The inset displays an interplanar distance of 4.77 Å, likely corresponding to the (101) lattice plane of tetragonal $GdVO_4$.

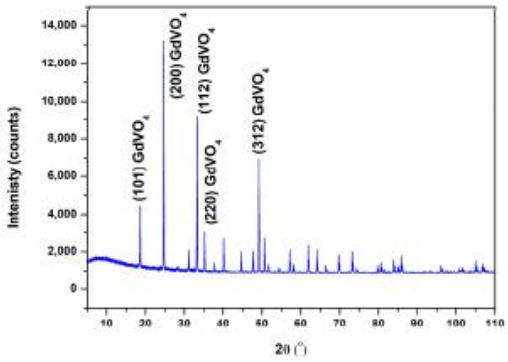

Figure 2. The XRD pattern of the $GdVO_4$-Sm nanopowder with respective Miller indices.

The particle size and morphology of the $GdVO_4$:Sm nanopowders were characterized by SEM (Figure 3). Some particles were agglomerated as clusters; however, individual spherical shaped particles are also visible in Figure 3. The estimated average particle size was about 50 nm. Looking at the SEM image (Figure 3), it is likely that the sizes of individual particles of nanopowders were about from 30 nm and up to 100 nm.

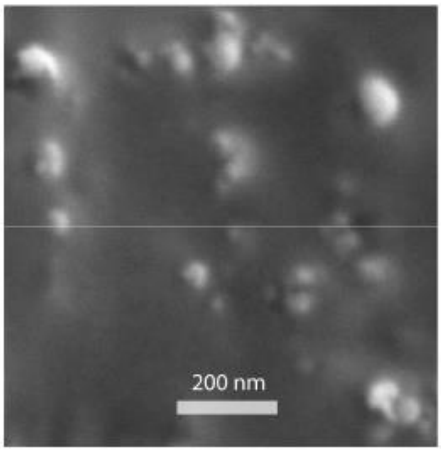

Figure 3. SEM image of $GdVO_4$:Sm nanopowder.

3.2. *Photoluminescence and Lifetime Analysis*

The streak image of the time-resolved photoluminescence spectrum of $GdVO_4$:Sm^{3+} using the 330 nm excitation is presented in Figure 4. The horizontal scale of the streak image corresponds to wavelength and the vertical scale shows the development of spectra in time. Images are usually presented in pseudocolor, where different colors mean different optical intensities. Using camera software, it was determined that the estimated lifetime of the most prominent samarium optical emission from the $^4G_{5/2}$ level is 0.78 ms at room temperature [1].

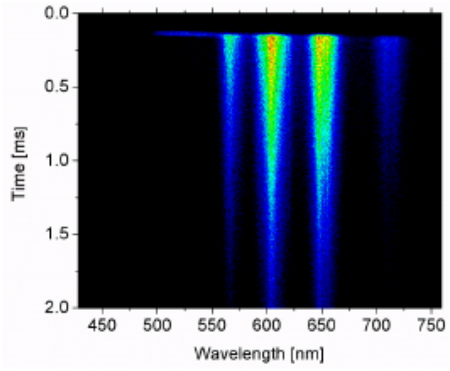

Figure 4. Streak image of the photoluminescence spectrum of $GdVO_4:Sm^{3+}$ nanophosphor (OPO excitation at 330 nm) at room temperature.

3.3. Photoluminescence and Lifetime Analysis Temperature Dependence of Photoluminescence

The new concept based on using the host luminescence for the luminescence intensity ratio method was introduced; for more details, see [4] and references therein. In our previous study [1], the method was improved by introducing temporal dependence in the intensity ratio measurements, as proposed in ref. [7]. Namely, it was possible to increase the sensitivity of the curve of intensity ratio between the host and samarium luminescence if the appropriately selected part of temporal evolution is used in calculation. This was our early attempt to improve the temperature estimation by introducing the temporal characteristics of luminescence emission, recorded by the streak camera. In ref. [25], we combined several methods for temperature measurements to obtain the best results.

The luminescence spectra of $GdVO_4$:Sm nanopowder were measured at various temperatures using OPO excitation at 330 nm and streak camera. Figure 5 shows the luminescence emission of $GdVO_4$:Sm nanopowder at two temperatures.

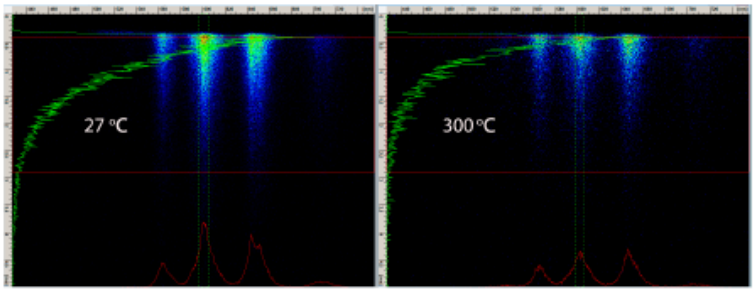

Figure 5. Streak images of the photoluminescence spectrum of $GdVO_4:Sm^{3+}$ nanophosphor at two temperatures.

Figure 6, which provides analysis of temperature dependence at eight different temperatures, is used in other analyses in this manuscript. Figure 6a shows changes in intensity ratios of luminescence peaks. Figure 6b shows and summarizes changes in luminescence lifetimes.

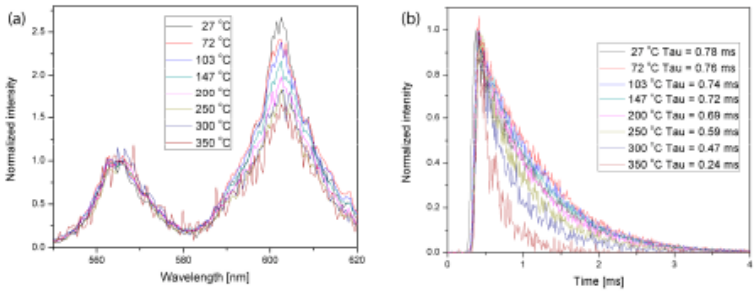

Figure 6. Temperature dependence of intensity ratios of luminescence peaks (**a**). Temperature dependence of luminescence lifetimes (**b**).

It can be seen in Figures 5 and 6 that intensity ratios between different peaks vary with changing the temperature of the sample. Moreover, lifetimes of luminescence emission decreases with the increase in temperature. So, it is intuitively clear that taking into account the intensity ratio and the lifetime of the luminescence emission provides better temperature estimation. The analysis will be further improved if the intensities of all prominent peaks are included into temperature estimation. The natural answer to the question of how to achieve all this is to use machine learning methods applied to streak images.

In this study, the spectra were measured at 640 wavelength points. The time axis of a streak image has 480 points. To alleviate the computational burden of machine learning computations, we selectively chose specific portions of the streak image that contained the majority of the spectral and time-resolved information. After some experimenting, for the ML analysis, we focused on 90 spectral points corresponding to bands between 558 nm and 568 nm, 592 nm and 612 nm, and 641 nm and 656 nm. The selected time frame consisted of 120 points. A total of 80 points were from a streak image with the time range of 100 µs, equivalent to approximately $80 \times 100/480 = 16.66$ µs, starting from 25 µs. Another 40 points dwere from a streak image (of the same sample at the same temperature) with the time range of 5 ms, equivalent to approximately $40 \times 5000/480 = 416.66$ µs, starting from 826 µs. In this way, there was sufficient information to highlight the intensity ratios and temporal decrease in luminescence. We see the omitted points as a computational burden, because in our earlier attempts, with larger ROIs, there were no increases in performance of the deep leaning network, just longer computational time.

To understand the following improvement of neural network performance, let us point out that the rows of the streak image correspond to the spectra of the image at a certain time, defined by the columns of the streak image. So, further improvement in performance was achieved when we replaced five rows of selected ROI with one row. In other words, each pixel of the new row was calculated as a mean value of five points of the same wavelength successive in time. Thus, we obtained an increased performance of the neural network (in a sense of root standard errors) because of the mean filtering of columns; moreover, we obtained calculations faster because of the reduced numbers of rows.

As a result, each sample used for ML analysis comprised $120/5 \times 90 = 24 \times 90 = 2160$ data points. To generate the input vector of 2160 data points, the pixel rows of each of the selected spectral bands in the image were packed sequentially in time row by row. In SOLO software, we used also two preprocessing techniques on neural network input: data, normalization, and data smoothing.

In order to construct the temperature calibration curve presented in ref. [1], we conducted measurements on samples at regular intervals of about 50 degrees Celsius, ranging from 27 °C to 350 °C. Measurements for temperature estimation were performed at two time ranges, 100 µs and 5 ms. However, the number of measurements was obviously insufficient for ML training. To obtain the larger training data set, we decided to use image

data augmenting techniques. A nice survey on image data augmentation for deep learning is presented in ref. [19].

As a clue to augmentation of our measured spectra, we used the experience from our earlier publication where measurements were carried out with the intention to be used for ML analysis, taking 50 streak images for each temperature. The visualization of these training data in ref. [18] by PCA and UMAP showed that the measured spectra at each temperature had similar characteristics. By looking at the spectral profiles, it could be seen that they were almost the same, differing only by random noise.

Here, we use the same spectra, measured in ref. [1]. In order to obtain augmented training set for ML analysis, we used the simple technique based on the properties of the acquired streak images. Keeping in mind that the luminescence lifetime of this material is about 0.78 ms, it is easy to see that translating the region of interest of a streak image by several rows results in almost negligible intensity change and a clear difference in random noise added by the photon counting mode. After selecting the region of interest for analysis, the shifting of the vertical offset of ROI was defined by a random number generator, serving the purpose of augmenting the training data set. The procedure was coded in the C language. We first used the training set consisting of 10 samples for each temperature. The training data for each temperature were added sequentially using batch processing to obtain a training data file readable by SOLO software.

To check the usefulness of constructed training set and the actual diversity of data, we used several visualization techniques.

Principal Component Analysis (PCA) score plots serve as a valuable tool for initial data assessment and verification. In Figure 7, the scores on the first three principal components of $GdVO_4$:Sm^{3+} spectra at different temperatures are displayed. It is noticeable that spectra obtained at similar temperatures tend to cluster together, although not perfectly. Consequently, to facilitate the initial data assessment, we incorporated t-Distributed Stochastic Neighbor Embedding (t-SNE) and Uniform Manifold Approximation and Projection (UMAP) clustering of $GdVO_4$:Sm^{3+} spectra at various temperatures.

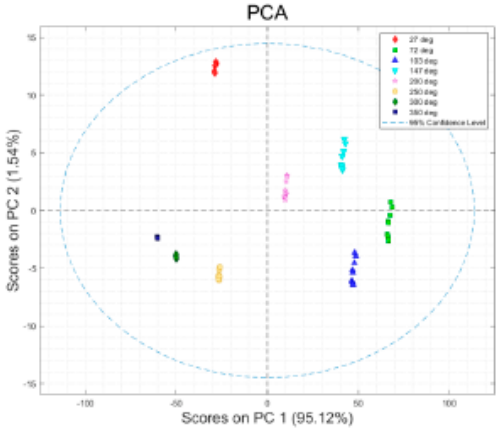

Figure 7. Scores on first two principal components of $GdVO_4$:Sm^{3+} spectra at different temperatures.

The t-SNE and UMAP clustering results of $GdVO_4$:Sm^{3+} spectra at various temperatures are depicted in Figures 8 and 9. It is obvious that the good groupings of classes are distinguishable.

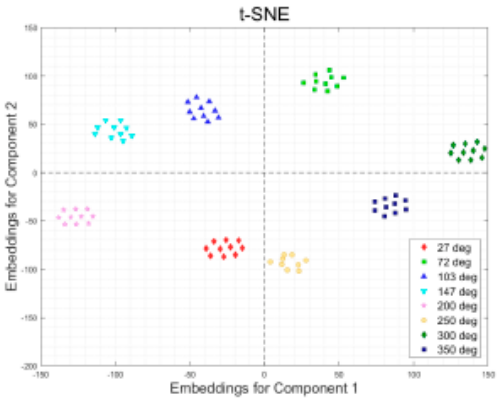

Figure 8. t-SNE component clustering of $GdVO_4:Sm^{3+}$ spectra at different temperatures.

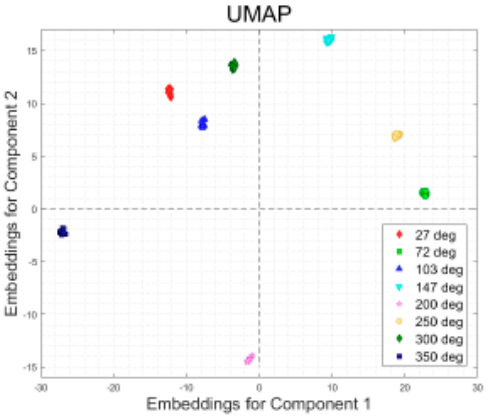

Figure 9. Uniform Manifold Approximation and Projection (UMAP) clustering of $GdVO_4:Sm^{3+}$ spectra at different temperatures.

The deep learning artificial neural network (ANNDL) implementation in SOLO can utilize either the SciKit or TensorFlow Python packages. In our case, we chose the TensorFlow Python package, which utilizes GPU acceleration for highly efficient computations.

The primary concept behind temperature estimation of thermophosphors using ANNDL involves training the network with sample spectra that have corresponding temperature measurements. During the training phase, the network iteratively minimizes errors between the calculated and predicted temperatures. Since the region of interest in the streak image of $GdVO_4:Sm^{3+}$ consists of 2160 points, the input layer of the deep learning network has 2160 nodes. Considering that this network aims to approximate two types of exponential functions—one for intensity ratios and another for luminescence lifetime—we initially considered using two hidden layers. The initial default size of a hidden layer in SOLO software is 100. However, we experimented with different numbers and sizes of hidden layers. Based on our experience, we decided that 100 nodes do not provide optimal predictions, in a sense of root mean standard errors. We gradually increased the sizes of hidden layers until the increase in neural network performance became saturated. Ultimately, we determined that a neural network with two hidden layers, each containing 540 nodes, was the optimal solution. The optimal number of epochs was 600, the batch size was 50. The output layer consisted of a single node representing the predicted temperature.

A schematic diagram illustrating the deep learning network used in this study is shown in Figure 10.

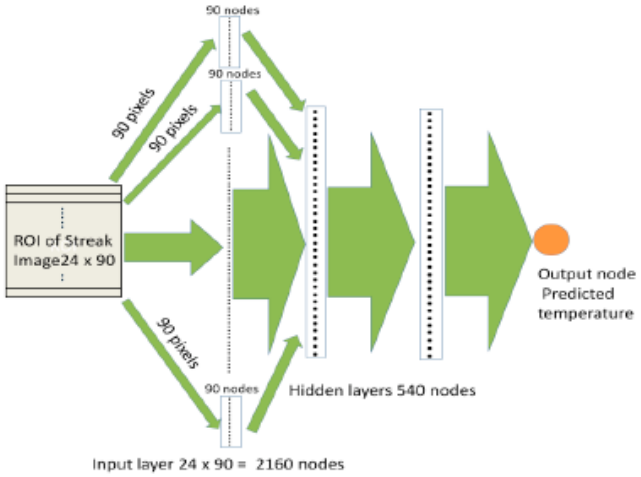

Figure 10. A schematic diagram illustrating the deep learning network used in this study. It is not possible to draw all arrows, and the shown arrows are merely symbolic. The pixel rows of the region of interest in the image are fed into the input layer as shown in the diagram.

After conducting several experiments, we determined that the *Adam* optimizer outperformed other optimizers, and that the *Relu* activation function is optimal for our case. *Adam* optimizer utilizes a default learning rate of 0.001, but it can adaptively adjust the learning rate based on the characteristics of the data. For cross-validation, we employed the Venetian blind method with a data split of 10, meaning that in each sub-validation experiment, 90% of the data was used for training and 10% for validation.

In other words, this 10% of data was used as test data, not seen by the computer in sub-validation experiment where 90% of data was used for training. To be precise, such sub-validation experiments were repeated 10 times, making test data unnecessary. Moreover, it should be noted that validation computational time is much longer than the initial construction of the neural network.

Following further experimentation, we selected a batch size of 50. After some trial and error, we decided to set the number of epochs to 600. Before processing the data, we used normalization procedure 1-Norm (area = 1) on the dataset. Then, the data were smoothed using the Savitzky–Golay filter. The width of the filter was five, with a polynomial order of six and weighted tails. These preprocessing options are built in the SOLO software.

Figure 11 shows the results of deep learning predictions of the measured temperatures when the neural network is presented with part of the spectra not seen by the computer in that validation cycle. Notably, the errors for the samples within the training set are relatively small. Validation errors are comparably larger. In comparison to the results presented in ref. [18], we observed larger maximum errors.

Based on the idea that a larger training set reduces problems in neural networks, we augmented the training set to 50 samples. Figure 12 shows the results of deep learning predictions of measured temperatures when the augmented training set was used. Moreover, optimizing the structure of the neural network resulted in decreasing of the optimal number of epochs from 600 to 100, and the batch size decreased from 50 to 12. Errors were comparable to the results presented in ref. [18].

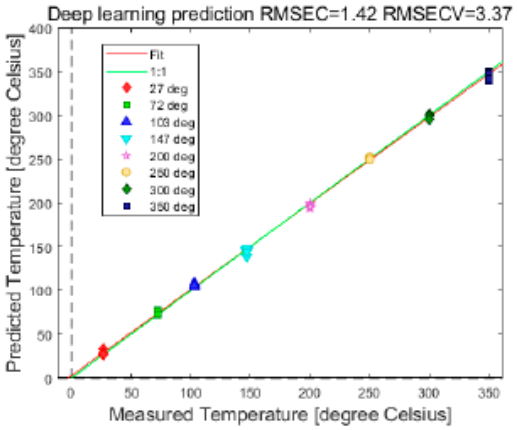

Figure 11. Plot of predicted temperatures using the training set of 10 samples for each temperature. RMSEC refers to the root mean standard error of calibration; RMSECV refers to the root mean standard error of cross-validation.

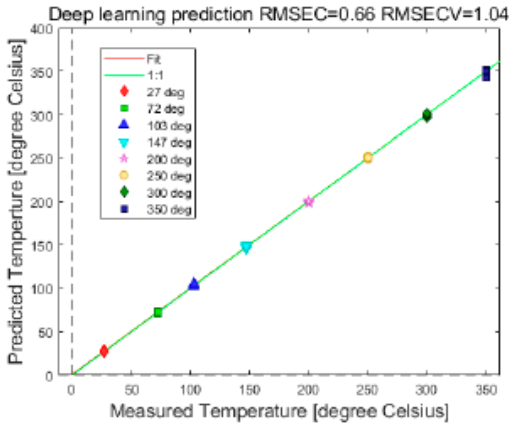

Figure 12. Plot of predicted temperatures using the training set of 50 samples for each temperature. RMSEC refers to the root mean standard error of calibration; RMSECV refers to the root mean standard error of cross-validation.

4. Discussion

In this study, the data not originally intended for ML were visualized using PCA, t-SNE, and UMAP, showing the good grouping of the data corresponding to the same temperature. Thus, in this paper, visualization techniques proved the possibility of using the original experimental data after appropriate augmentation.

In [18], for each temperature, a set of 50 spectra was measured, resulting in a total of 650 training spectra (13 temperatures multiplied by 50 spectra per temperature). Here, we analyzed the spectra corresponding to eight temperatures, and the training set initially comprised 80 (8 multiplied by 10) spectra. Using visualization techniques, we proved that the technique used for data augmentation was appropriate. However, subsequently using ANNDL to obtain temperature predictions with similar values of RMS as in ref. [18], we had to expand the training set up to 50 for each temperature. After that, the structure of ANNDL and computational times were similar to those in ref. [18]. It should be

pointed out that structure (number of hidden layers and number of their nodes), number of epochs, and batch size decreased when ANNDL was trained with the training set of 50 for each sample.

In the previous section, we presented the best results achieved through a trial-and-error process. Now, we validate this educated guess using the learning curves of the neural network. The learning curves illustrating the training progress of the ANNDL model are shown in Figure 13. The curves were generated by repeatedly running the deep neural network model with an increasing number of epochs. Based on the shapes of these curves, we decided to set the number of epochs for future experiments with these data to 100 as a precaution.

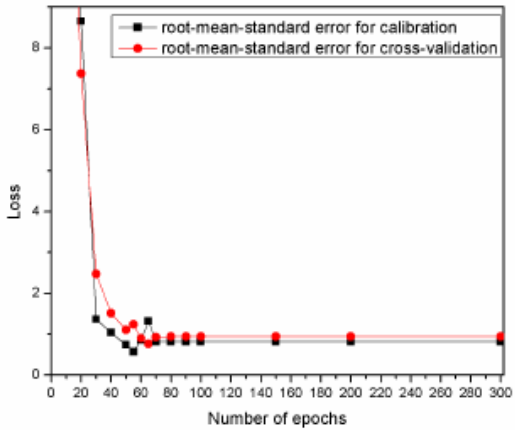

Figure 13. The learning curves depicting the training progress of the ANNDL model.

When comparing our results to those reported in ref. [26], our method yields slightly superior prediction errors. Notably, our deep neural network model achieves optimal performance after approximately 100 epochs, whereas the study in ref. [26] requires training the network for 6000 epochs.

In reference [13], the authors explore the use of linear transformations (Principal Component Analysis) and non-linear transformations (t-Distributed Stochastic Neighbor Embedding) on thermophosphor calibration datasets. Their findings show a clear advantage compared to our results when using PCA or UMAP. However, this was exactly why we chose to employ a deep learning neural network in our approach.

Compared to the results presented in ref. [12], we observed slightly larger maximum errors. We anticipated that incorporating the time development of luminescence spectra into our prediction model would enhance performance relative to the network described in ref. [12]. However, it is important to note that our temperature controller lacks manufacturer-specified resolution and accuracy. We estimate that its sporadic errors can reach up to two degrees Celsius, regardless of the temperature value. As a result, the relative error can be significant at lower temperatures. In contrast, the temperature controller used in ref. [12] has a specified temperature resolution of 0.01 degrees Celsius and a stability of ±0.05 degrees Celsius. Our main objective was to validate the concept of using the time evolution of luminescence spectra for remote temperature estimation, and the results presented here support this concept.

5. Conclusions

After phase identification and morphology of post-annealed powder samples $GdVO_4$:Sm^{3+} using X-ray diffraction, the time-resolved analysis of this nanoposphor luminescence was conducted. The estimated lifetime of the most prominent samarium optical

emission from the $^4G_{5/2}$ level is 0.726 ms at room temperature. We employed machine learning techniques to analyze the optical spectra of $GdVO_4$:Sm^{3+} thermophosphor in order to improve remote temperature measurements. Our approach deviates from the conventional method of identifying spectral peaks and calculating their intensity ratio. Instead, we trained a computer model to recognize the time-resolved spectra associated with different temperatures of the thermophosphors. This allowed us incorporation of not only the intensity ratios of all peaks but also the luminescence lifetime as an additional parameter. We showed that, for the analyzed $GdVO_4$:Sm^{3+} material, the temperature sensing is useful up to 350 °C. We used the streak camera to prove the concept. The real application of this method will be based on using the gated CCD cameras and appropriate bandwidth filters for selecting the emission region of interest. To improve the performance of the deep learning network, we used the augmenting of the training data set. In summary, our analyses proved that it is possible to use a deep learning neural network for improved temperature sensing with Sm^{3+}-doped $GdVO_4$ nanopowder.

Author Contributions: Conceptualization, D.S., M.S.R. and M.G.N.; software, D.S.; formal analysis, A.D. and J.Z.J.; investigation, D.S., M.S.R. and M.D.R.; resources, J.K., M.H.A. and S.S.-S.; writing—original draft preparation, D.S. and M.S.R.; writing—review and editing, D.S., M.S.R. and M.D.R. All authors have read and agreed to the published version of the manuscript.

Funding: This work was financially supported by funding provided by the Institute of Physics Belgrade, through the grant by the Ministry of Science, Technological Development and Innovations of the Republic of Serbia and by European Commission through Marie Skłodowska-Curie Actions H2020 RISE with ULTIMATE-I (Grant No. 101007825). Authors would like to acknowledge the access of equipment of "Servicio General de Apoyo a la Investigación (SAI), Univesidad de Zaragoza".

Data Availability Statement: The original contributions presented in the study are included in the article, further inquiries can be directed to the corresponding author/s.

Conflicts of Interest: The authors declare no conflicts of interest.

References

1. Rabasovic, M.S.; Krizan, J.; Savic-Sevic, S.; Mitric, M.; Rabasovic, M.D.; Marinkovic, B.P.; Sevic, D. Orange-Reddish Light Emitting Phosphor $GdVO_4$:Sm^{3+} Prepared by Solution Combustion Synthesis. *J. Spectrosc.* **2018**, *2018*, 1–8. [CrossRef]
2. Nikolić, M.G.; Jovanović, D.J.; Đorđević, V.; Antić, Ž.; Krsmanović, R.M.; Dramićanin, M.D. Thermographic properties of Sm^{3+}-doped $GdVO_4$ phosphor. *Phys. Scr.* **2012**, *T149*, 014063. [CrossRef]
3. Nikolić, M.G.; Antić, Ž.; Ćulubrk, S.; Nedeljković, J.M.; Dramićanin, M.D. Temperature sensing with Eu^{3+} doped TiO_2 nanoparticles. *Sens. Actuators B Chem.* **2014**, *201*, 46–50. [CrossRef]
4. Dramićanin, M.D.; Antić, Ž.; Ćulubrk, S.; Ahrenkiel, S.P.; Nedeljković, J.M. Self-referenced luminescence thermometry with Sm3+ doped TiO_2 nanoparticles. *Nanotechnology* **2014**, *25*, 485501. [CrossRef] [PubMed]
5. Lojpur, V.; Nikolić, M.G.; Jovanović, D.; Medić, M.; Antić, Ž.; Dramićanin, M.D. Luminescence thermometry with Zn_2SiO_4:Mn^{2+} powder. *Appl. Phys. Lett.* **2013**, *103*, 141912. [CrossRef]
6. Lojpur, V.; Ćulubrk, S.; Dramićanin, M.D. Ratiometric luminescence thermometry with different combinations of emissions from Eu^{3+} doped $Gd_2Ti_2O_7$ nanoparticles. *J. Lumin.* **2016**, *169*, 534–538. [CrossRef]
7. Aldén, M.; Omrane, A.; Richter, M.; Särner, G. Thermographic phosphors for thermometry: A survey of combustion applications. *Prog. Energy Combust. Sci.* **2011**, *37*, 422–461. [CrossRef]
8. Chatzidakis, M.; Botton, G.A. Towards calibration-invariant spectroscopy using deep learning. *Sci. Rep.* **2019**, *9*, 2126. [CrossRef]
9. Dramićanin, T.; Zeković, I.; Periša, J.; Dramićanin, M.D. The Parallel Factor Analysis of Beer Fluorescence. *J. Fluoresc.* **2019**, *29*, 1103–1111. [CrossRef]
10. Ranamukhaarachchi, S.A.; Peiris, R.H.; Moresoli, C. Fluorescence spectroscopy and principal component analysis of soy protein hydrolysate fractions and the potential to assess their antioxidant capacity characteristics. *Food Chem.* **2017**, *217*, 469–475. [CrossRef]
11. Weng, S.; Yuan, H.; Zhang, X.; Li, P.; Zheng, L.; Zhao, J.; Huang, L. Deep learning networks for the recognition and quantitation of surface-enhanced Raman spectroscopy. *Anal.* **2020**, *145*, 4827–4835. [CrossRef]
12. Cui, J.; Xu, W.; Yao, M.; Zheng, L.; Hu, C.; Zhang, Z.; Sun, Z. Convolutional neural networks open up horizons for luminescence thermometry. *J. Lumin.* **2023**, *256*, 119637. [CrossRef]
13. Ximendes, E.; Marin, R.; Carlos, L.D.; Jaque, D. Less is more: Dimensionality reduction as a general strategy for more precise luminescence thermometry. *Light Sci. Appl.* **2022**, *11*, 237. [CrossRef]

14. Barbon, S.; da Costa Barbon, A.P.A.; Mantovani, R.G.; Barbin, D.F. Machine Learning Applied to Near-Infrared Spectra for Chicken Meat Classification. *J. Spectrosc.* **2018**, *2018*, 1–12. [CrossRef]
15. Geronimo, B.C.; Mastelini, S.M.; Carvalho, R.H.; Barbon Júnior, S.; Barbin, D.F.; Shimokomaki, M.; Ida, E.I. Computer vision system and near-infrared spectroscopy for identification and classification of chicken with wooden breast, and physicochemical and technological characterization. *Infrared Phys. Technol.* **2019**, *96*, 303–310. [CrossRef]
16. Junior, S.B.; Mastelini, S.M.; Barbon, A.P.A.; Barbin, D.F.; Calvini, R.; Lopes, J.F.; Ulrici, A. Multi-target prediction of wheat flour quality parameters with near infrared spectroscopy. *Inf. Process. Agric.* **2020**, *7*, 342–354. [CrossRef]
17. Nolasco Perez, I.M.; Badaró, A.T.; Barbon, S.; Barbon, A.P.A.; Pollonio, M.A.R.; Barbin, D.F. Classification of Chicken Parts Using a Portable Near-Infrared (NIR) Spectrophotometer and Machine Learning. *Appl. Spectrosc.* **2018**, *72*, 1774–1780. [CrossRef] [PubMed]
18. Rabasovic, M.S.; Savic-Sevic, S.; Križan, J.; Matovic, B.; Nikolic, M.; Sevic, D. Time resolved study of temperature sensing using Gd_2O_3:Er,Yb: Deep learning approach. *Phys. Scr.* **2023**, *98*, 116003. [CrossRef]
19. Shorten, C.; Khoshgoftaar, T.M. A survey on Image Data Augmentation for Deep Learning. *J. Big Data* **2019**, *6*, 60. [CrossRef]
20. Rabasović, M.D.; Murić, B.D.; Čelebonović, V.; Mitrić, M.; Jelenković, B.M.; Nikolić, M.G. Luminescence thermometry via the two-dopant intensity ratio of Y_2O_3:Er^{3+}, Eu^{3+}. *J. Phys. D Appl. Phys.* **2016**, *49*, 485104. [CrossRef]
21. Hotelling, H. Analysis of a complex of statistical variables into principal components. *J. Educ. Psychol.* **1933**, *24*, 417–441. [CrossRef]
22. Wise, B.M.; Gallagher, N.B.; Bro, R.; Shaver, J.M.; Windig, W.; Koch, R.S. *Chemometrics Tutorial for PLS Toolbox and Solo*; Eigenvector Research, Inc.: Wenatchee, WA, USA, 2006; ISBN 0-9761184-1-6.
23. Van der Maaten, L.; Hinton, G. Visualizing data using t-SNE. *J. Mach. Learn. Res.* **2008**, *9*, 2579.
24. McInnes, L.; Healy, J.; Saul, N.; Großberger, L. UMAP: Uniform Manifold Approximation and Projection. *J. Open Source Softw.* **2018**, *3*, 861. [CrossRef]
25. Sevic, D.; Rabasovic, M.S.; Krizan, J.; Savic-Sevic, S.; Nikolic, M.G.; Marinkovic, B.P.; Rabasovic, M.D. YVO_4:Eu^{3+} nanopowders: Multi-mode temperature sensing technique. *J. Phys. D Appl. Phys.* **2020**, *53*, 015106. [CrossRef]
26. Lewis, C.; Erikson, J.W.; Sanchez, D.A.; McClure, C.E.; Nordin, G.P.; Munro, T.R.; Colton, J.S. Use of Machine Learning with Temporal Photoluminescence Signals from CdTe Quantum Dots for Temperature Measurement in Microfluidic Devices. *ACS Appl. Nano Mater.* **2020**, *3*, 4045–4053. [CrossRef]

Contrib. Astron. Obs. Skalnaté Pleso **53/3**, 115 – 124, (2023)
https://doi.org/10.31577/caosp.2023.53.3.115

Data of plasma velocity obtained from Streak image processing of laser-induced breakdown

M.S. Rabasovic, A. Dencevski, M.D. Rabasovic and D. Sevic

Institute of Physics Belgrade, University of Belgrade, Pregrevica 118, 11080 Zemun, Serbia, (E-mail: sevic@ipb.ac.rs)

Received: September 30, 2023; Accepted: November 6, 2023

Abstract. We present time resolved measurements of the laser induced plasma development in air. A Q-switched Nd:YAG laser is employed as the excitation source. The detection part of the acquisition system is based on a streak camera. We propose streak image processing technique based on a set of simple algorithms as a way to obtain estimations of plasma core and plasma plume instantaneous velocity. Using of the proposed technique enables us to obtain all data relevant for temporal analysis by a single shot excitation.

Key words: Laser induced breakdown spectroscopy – Streak camera – Image processing

1. Introduction

The formation of laser induced breakdown (LIB) refers to a plasma production by focusing an intense laser beam in a gas, liquid or solid target. Parameters of laser induced plasma depend on irradiation conditions, such as laser intensity, pulse duration, laser wavelength or ambient gas. To understand the process of laser induced breakdown it is required to obtain the detailed knowledge of the initial stages of various processes involving laser duration and irradiation, plasma formation and its expansion. The nanosecond laser pulse generates plasma through thermal and non-thermal mechanisms. Studying the plasma formation with a high temporal, spectral and spatial resolution is of a great interest and formation of laser induced breakdown plasma in air has been studied by many researchers Robledo-Martinez et al. (2008); Villagran-Muniz et al. (2001); Camacho et al. (2010); Kawahara et al. (2007); Pandey & Thareja (2010); Hori & Akamatsu (2008), including references therein. After the initial breakdown, plasma plume propagates towards the focusing lens Robledo-Martinez et al. (2008). The bright plasma core of the LIB plasma in open air is surrounded by a layer of cold, moderately ionized gas called the sheath Robledo-Martinez et al. (2008). Glow of plasma sheath, although fainter than the core, is also visible to the naked eye. An explosive plasma expansion induces optodynamic phenomena, i.e., the propagation of a shock, acoustical and ultrasonic waves. The optodynamic phenomena convey important information about the

laser-material interaction. On the other hand, optical lines emission due to the electron transitions in laser-induced plasma can be used to obtain the crucial information for elemental analysis of samples in all three states. Studying the plasma formation with a high temporal and spatial resolution is therefore of a great importance in a laser-induced material transfer Bohandy et al. (1986); Mattle et al. (2012); Feinaeugle et al. (2012), pulsed-laser deposition Lunney (1995); Sánchez-Aké et al. (2012); Guzmán et al. (2013), and various industrial applications Bilmes et al. (2006); Lackner et al. (2004). The velocity field measurement of LIB plasma plumes in air has been the subject of various experimental techniques in recent years Koll et al. (2020); Shi et al. (2019); Nishihara et al. (2020). The influence of the delay time between the subsequent plasma images along the different directions are investigated in Shi et al. (2019). In this paper we propose streak image processing technique as a way to obtain estimations of plasma core and plasma plume periphery instantaneous velocity. Studies with similar aims were presented in references Robledo-Martinez et al. (2008); Villagran-Muniz et al. (2001); Camacho et al. (2010); Kawahara et al. (2007), but our method of data processing is quite different. Using the picosecond temporal resolution of our streak camera we analyze the initial time period after the laser induced breakdown. There are many well known simple image processing algorithms but the answer to the question which simple algorithms should be selected for use and how to combine them to achieve the goal desired in our study is not simple at all. After some considerations we discarded several techniques which seemed at the first glance as obvious solution for our problem. Namely, common image processing techniques are usually intended to be used on images seen in nature by a human observer. Streak images look like images, but they have some specific characteristics. First of all, they are spatial only in one dimension, the other dimension being the time. So, for example, general gradient methods for image edge detection would be misused if applied here and we discarded them.

2. Methods

A schematic diagram of the experimental apparatus is shown in Fig. 1. Time resolved LIB system implemented in our laboratory is based on Nd:YAG laser and Optical Parametric Oscillator (OPO; Vibrant 266). The OPO system, pumped by a pulsed Q switched Nd:YAG laser (Brilliant B) includes the second and fourth harmonic generator (SHG and FHG). In our experiments we used all outputs of this laser system as the excitation sources, but in this paper only the fundamental output at 1064 nm (pulse energy up to 270 mJ, pulse duration of about 5 ns) is used to create an optical breakdown in ambient air. One of advantages of using the excitation at 1064 nm is the fact that, for any kind of temporal analysis, we do not need to perform deconvolution of the laser pulse signal from streak image of plasma emission. The delay generator (Stanford Re-

search Systems DG535) plays a significant role in the streak camera operation. Timing considerations regarding the laser pulse and streak camera synchronization are very important in our measurements Rabasovic et al. (2012, 2019), so we added a photodiode and digital oscilloscope to our experimental setup, Fig. 1. The plasma plume in air is obtained by focusing the laser beam using lens with the focal length of 40 mm. The OPO system is controlled by OPOTEK software installed on PC.

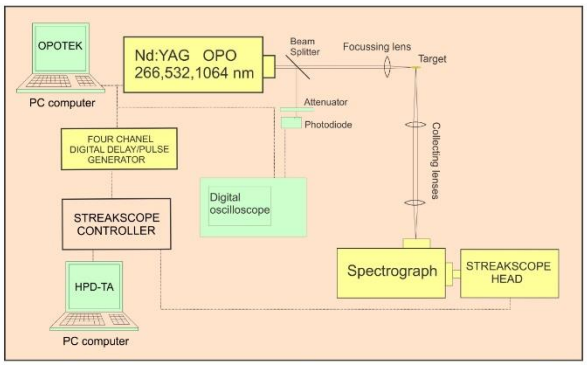

Figure 1. Setup for time-resolved laser induced breakdown measurements.

The optical emission from the plasma is collected by using a spectrograph (SpectraPro 2300i) and recorded with a Hamamatsu streak camera (model C4334) (Fig. 1). The streak images are time resolved thus enabling monitoring of temporal evolution of the ionic and atomic emission lines or spatial development of the plasma. The camera has the spectral range from 200 nm to 850 nm and time resolution up to 30 ps. The CCD chip has a resolution of 640 x 480 pixels. The data are acquired and analyzed using High Performance Digital Temporal Analyzer (HPD-TA) software, provided by Hamamatsu. Our earlier research of optical emission of plasma was limited so far to analysis of time resolved optical emission spectra acquired by the streak camera Sevic et al. (2011); Rabasovic et al. (2012, 2014). To make our study more comprehensive we saw the need for measuring the spatial distribution of plasma optical emission Rabasovic et al. (2019) and requirement for easy switching between the spectral and spatial measurement modes of our streak camera system soon became apparent to us. We performed a simple modification of our spectrograph that enables easy switching between the spectral and spatial measurement modes. Similar modification was already proposed and successfully used in the study of Siegel et al. (2005), where imaging device was ICCD camera. Our modifica-

tion is different in a sense that optical alignment of target area to the streak camera slit needs special consideration and careful procedure. The spectrograph contains the triple grating turret. The diffraction gratings of 50, 150 and 300 gr/mm were installed. In the place of the 150 gr/mm grating we mounted the plain mirror. Now, if grating of 150 gr/mm is selected by HPD-TA software, than spectromemer projects the image of entrance slit to the streak camera. At the same time, collecting lenses project the image of the target plasma to the spectrometer entrance slit. In this way, streak camera instead of the image of the optical spectrum takes the image of the spatial distribution of the optical emission of the laser induced breakdown. The spectrograph entrance slit should be fully open to utilize as much as possible of the CCD camera active area. For measurements presented here other optical parts of the acquisition system were chosen so to have overall optical magnification of 0.6. In this case, the calibration procedure shows that 1 mm on the target position corresponds to 72 pixels of the CCD camera.

3. Results and discussion

Single-shot laser induced breakdown plasma emission spatial images analyzed in this paper are acquired in the direction perpendicular to the laser beam, as shown in Fig. 1. The streak image of the laser induced plasma (excitation at 1064 nm, energy of 51 mJ, peak intensity of 1.3 10^{11} W/cm^2) is shown in Fig. 2. The time axis is vertical, with zero time on the top of the image. The spatial axis is horizontal. The development of the plasma is seen on the streak image as vertical development (corresponding to a passing of time) of a narrow horizontal section of plasma optical emission, seen through the camera slit, along the direction of propagation of the laser beam. In other words, two dimensional (2 D) streak image corresponds to only 1-D spatial image, represented by rows of image matrix, the other dimension being the time. The streak images are often presented in pseudo-color, where different intensities are coded as different colors. However, the edges on such images could be misunderstood by an observer, so we present streak image as grayscale. Red points indicate the edges and peak values of plasma brightness, detected by our image processing algorithm. The laser beam is incident from the right-hand side of the streak image. As expected Robledo-Martinez et al. (2008), plasma plume expands towards the laser beam.

Our streak image processing algorithm is effective and easy to implement. First, the rows of streak image are mean filtered, using nine neighboring pixels, two times iteratively.

$$Lout[x] = \frac{\sum_{x=-4}^{x=4} L[x]}{9.0} \tag{1}$$

where $L[x]$ denotes intensity of streak image pixel with coordinate x.

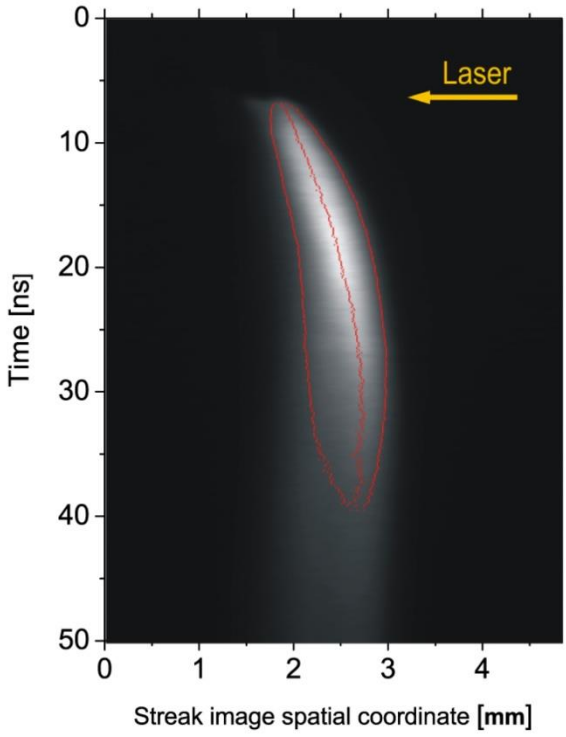

Figure 2. Streak image of the laser induced plasma (excitation at 1064 nm, energy of 51 mJ). Red points indicate the detected edges and peak values of brightness of the plasma plume.

The preliminary tests showed that mean filter is quite satisfying and simple method of filtering. We didn't use median filter because it is not suitable for Gaussian noise which is present on our streak images. It is generally true that median filter (often improved with several techniques like fuzzy logic, weighted coefficients, etc) performs better than mean filter. However, when there is too much Gaussian noise, a median filter blurs fine structures of an image and causes edge jitter and streaking Yang (1999). So, after some initial tries we have selected the mean filter which is simpler to implement than median. To alleviate effects of impulse noise, we introduced the following correcting rule:

if $((L[x] - mean) > threshold)$ then $L[x] = mean$
where $mean$ is calculated as mean value of eight neighboring s:

$$mean = \frac{\sum_{x=-4}^{x=-1} L[x] + \sum_{x=1}^{x=4} L[x]}{8.0} \tag{2}$$

After some experimenting, The *threshold* was set to be 5 % of value of maximal pixel intensity of analyzed streak image.

The problem of streak image noise is typically solved by using some kind of cumulative or integrating measuring streak camera techniques, based on repetitive laser excitation. By using the proposed filtering method it is possible to use a single-shot laser excitation.

All our streak images of plasma development are of the similar shape and the plasma contour is similarly positioned on the image, so it is possible to use a simplified algorithm for edge detection, specialized for our purpose. Namely, it is assumed that the right edge of plasma plume is detected when pixel intensities exceeds certain threshold above the averaged background, testing iteratively through the row of pixels, starting from the right side of the image. The algorithm is similarly conducted for the left edge of plasma plume. It is supposed that the pixel or pixels with the peak value of brightness of plasma core are identified when the value of pixel is equal to the calculated value of peak of that row. We did not limit the peak to the only one pixel because it would make a fitting of curve indicating the moving of plasma core more difficult.

The time diagrams of position changes of left and right side edge of plasma plume, and of the peak of plasma brightness, corresponding to the movement of the center of plasma core, are shown in Fig. 3. Note that the time ranges in Figures 3 and 4 correspond to the part of streak image where plasma expands. The diagrams are obtained by transferring the coordinates of pixels corresponding to detected edges and peaks of rows of streak image from Fig. 2. Time dependence of instantaneous-velocity of edges of plasma plume and peak brightness were also calculated from the same data set and shown in Fig. 4. Data corresponding to fitted curves from Fig. 3 were used for calculation to avoid nonexistent velocity fluctuations. Because the plasma plume is expanding and moving to the right at the same time, the velocity of the right edge is greater than the velocity of the center of the core, as shown in Fig. 4. As the expansion of the plasma plume ceases (for excitation energy of 51 mJ after about 10 ns) the velocity of right edge of plasma plume decreases. The velocity of the left edge of the plasma plume is smallest, because the direction of the plasma expanding is opposite to the direction of the plasma moving (Fig. 4).

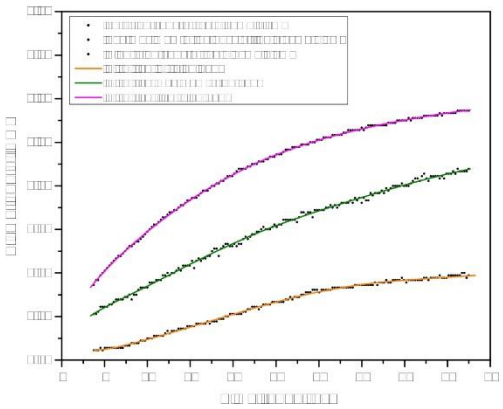

Figure 3. The time diagrams of moving of left side and right side edge of plasma plume, and of the peak of plasma brightness.

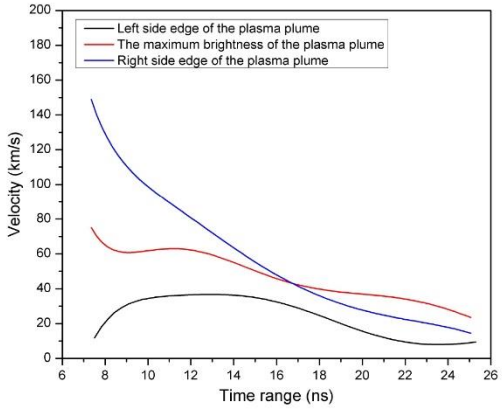

Figure 4. The time diagrams of instantaneous velocity of left side, right side (towards the laser beam) edge of plasma plume, and of the peak of plasma brightness.

Let us point out that, as stated in Introduction, our approach is quite different than the approaches in references describing investigations of laser produced plasma plume cited in our paper (before all, because their experimental equipment is more complex), so it is difficult to provide a quantitative comparison. There is no doubt that the results presented in cited references are more detailed and reliable, but similar investigations in cited references use fast framing cameras with two dimensional imaging, while our streak camera, although faster in time, has only one spatial dimension. Our study provides improved analysis of streak images based on image processing techniques.

It's important to highlight that the single-shot feature of our system has two dimensions: firstly, all the necessary data for calculating instantaneous velocity can be found within a single streak image, and secondly, the streak image can be acquired in a single shot thanks to the noise filtering method introduced in this paper.

4. Discussion and Conclusions

We have presented streak camera velocity measurements of the laser induced plasma development in air. We have described how to obtain estimations of plasma core and sheath instantaneous velocity by using streak image processing technique, based on image noise filtering and plasma sheet edge and plasma core peak brightness detection. So, we have provided, by data postprocessing techniques, alternative to much more complex experimental setups analyzing the laser produced plasma plume. All data relevant for temporal analysis were acquired by a single shot excitation. The presented method is suitable for plasma sheath velocity measurements from the very beginning of the laser induced breakdown by using a picosecond time resolution of our streak camera. For our future work we plan to include machine learning techniques for improving quality of streak images.

Acknowledgements. This work was financially supported by funding provided by the Institute of Physics Belgrade, through the grant by the Ministry of Science and Technological Development of the Republic of Serbia.

References

Bilmes, G. M., Orzi, D. J. O., Martínez, O. E., & Lencina, A., A real time method for surface cleanliness measurement. 2006, *Applied Physics B: Lasers and Optics*, **82**, 643, DOI: 10.1007/s00340-005-2096-7

Bohandy, J., Kim, B. F., & Adrian, F. J., Metal deposition from a supported metal film using an excimer laser. 1986, *Journal of Applied Physics*, **60**, 1538, DOI: 10.1063/1.337287

Camacho, J. J., Díaz, L., Santos, M., Juan, L. J., & Poyato, J. M. L., Time-resolved optical emission spectroscopy of laser-produced air plasma. 2010, *Journal of Applied Physics*, **107**, 083306, DOI: 10.1063/1.3382914

Feinaeugle, M., Alloncle, A. P., Delaporte, P., Sones, C. L., & Eason, R. W., Time-resolved shadowgraph imaging of femtosecond laser-induced forward transfer of solid materials. 2012, *Applied Surface Science*, **258**, 8475, DOI: 10.1016/j.apsusc.2012.04.101

Guzmán, F., Favre, M., Ruiz, H. M., et al., Pulsed laser deposition of thin carbon films in a neutral gas background. 2013, *Journal of Physics D Applied Physics*, **46**, 215202, DOI: 10.1088/0022-3727/46/21/215202

Hori, T. & Akamatsu, F., Laser-Induced Breakdown Plasma Observed using a Streak Camera. 2008, *Japanese Journal of Applied Physics*, **47**, 4759, DOI: 10.1143/JJAP.47.4759

Kawahara, N., Beduneau, J. L., Nakayama, T., Tomita, E., & Ikeda, Y., Spatially, temporally, and spectrally resolved measurement of laser-induced plasma in air. 2007, *Applied Physics B: Lasers and Optics*, **86**, 605, DOI: 10.1007/s00340-006-2531-4

Koll, M., Freund, J. B., & Elliott, G. S., Particle Image Velocimetry of a Nano-Second Laser-Induced Breakdown in Air. 2020, *AIAA Scitech 2020 Forum, Session: Other Topics in Fluid Dynamics III*, 1, DOI: 10.2514/6.2020-2047

Lackner, M., Charareh, S., Winter, F., et al., Investigation of the early stages in laser-induced ignition by Schlieren photography and laser-induced fluorescence spectroscopy. 2004, *Optics Express*, **12**, 4546, DOI: 10.1364/OPEX.12.004546

Lunney, J. G., Pulsed laser deposition of metal and metal multilayer films. 1995, *Applied Surface Science*, **86**, 79, DOI: 10.1016/0169-4332(94)00368-8

Mattle, T., Shaw-Stewart, J., Schneider, C. W., Lippert, T., & Wokaun, A., Laser induced forward transfer aluminum layers: Process investigation by time resolved imaging. 2012, *Applied Surface Science*, **258**, 9352, DOI: 10.1016/j.apsusc.2011.08.113

Nishihara, M., Freund, J. B., & Elliott, G. S., A study of velocity, temperature, and density in the plasma generated by laser-induced breakdowns. 2020, *Journal of Physics D Applied Physics*, **53**, 105203, DOI: 10.1088/1361-6463/ab5b26

Pandey, P. K. & Thareja, R. K., Plume dynamics of laser produced air plasma. 2010, in Journal of Physics Conference Series, Vol. **208**, *Journal of Physics Conference Series*, 012091

Rabasovic, M., Rabasovic, M., Marinkovic, B., & Sevic, D., Laser-Induced Plasma Measurements Using Nd:YAG Laser and Streak Camera: Timing Considerations. 2019, *Atoms*, **7**, 6, DOI: 10.3390/atoms7010006

Rabasovic, M. S., Marinkovic, B. P., & Sevic, D., Time-Resolved Optical Spectra of the Laser-Induced Indium Plasma Detected Using a Streak Camera. 2014, *IEEE Transactions on Plasma Science*, **42**, 2588, DOI: 10.1109/TPS.2014.2352400

Rabasovic, M. S., Sevic, D., Pejcev, V., & Marinkovic, B. P., Detecting indium spectral lines using electron and laser induced breakdown spectroscopy.

2012, *Nuclear Instruments and Methods in Physics Research B*, **279**, 58, DOI: 10.1016/j.nimb.2011.10.020

Robledo-Martinez, A., Sobral, H., Villagrán-Muniz, M., & Bredice, F., Light focusing from large refractive indices in ionized air. 2008, *Physics of Plasmas*, **15**, 093510, DOI: 10.1063/1.2988768

Sánchez-Aké, C., Camacho, R., & Moreno, L., Deposition and composition-control of Mn-doped ZnO thin films by combinatorial pulsed laser deposition using two delayed plasma plumes. 2012, *Journal of Applied Physics*, **112**, 044904, DOI: 10.1063/1.4747935

Sevic, D., Rabasovic, M., & Marinkovic, B. P., Time-Resolved LIBS Streak Spectrum Processing. 2011, *IEEE Transactions on Plasma Science*, **39**, 2782, DOI: 10.1109/TPS.2011.2158555

Shi, Z., Hardalupas, Y., & Taylor, A. M. K. P., Laser-induced plasma image velocimetry. 2019, *Experiments in Fluids*, **60**, 5, DOI: 10.1007/s00348-018-2649-2

Siegel, J., Epurescu, G., Perea, A., et al., High spatial resolution in laser-induced breakdown spectroscopy of expanding plasmas. 2005, *Spectrochimica Acta*, **60**, 915, DOI: 10.1016/j.sab.2005.05.020

Villagran-Muniz, M., Sobral, H., Sanchez Ake, C., Escobar, L., & Camps, E., Plasma ablation characterization by a laser beam deflection technique. 2001, in Society of Photo-Optical Instrumentation Engineers (SPIE) Conference Series, Vol. **4419**, *4th Iberoamerican Meeting on Optics and 7th Latin American Meeting on Optics, Lasers, and Their Applications*, ed. V. L. Brudny, S. A. Ledesma, & M. C. Marconi, 102–105

Yang, T. 1999, Advances in Imaging and Electron Physics, Vol. **109**, *Fuzzy Cellular Neural Networks and Their Applications to Image Processing*, ed. P. W. Hawkes (Elsevier), 265–446

retains its degree of dispersion for one week. Therefore, this model is a suitable candidate for further research and development of a lipid-based dosage form for Alendronate sodium.

S13-BMP-200 / **Poster presentation**

Determination of spatial resolution of nonlinear laser scanning microscopy

Authors: Aleksa Dencevski[1]; Jovana Jelic[1]; Marta Bukumira[1]; Aleksandar Krmpot[1]; Ana Senkic[2]; Antonio Supina[2]; Mihailo Rabasovic[1]; Natasa Vujicic[2]; Stanko Nikolic[1]

[1] *Institute of Physics Belgrade*

[2] *Institute of Physics Zagreb*

Presenter: M. Bukumira (marta@ipb.ac.rs)

Microscope resolution is the shortest distance between two points on a sample that can be distinguished as separate entities. Due to the wave nature of light and the phenomenon of diffraction, it is fundamentally limited: even under theoretically ideal conditions and optical components, the microscope has a finite resolution.

In this paper, we determined lateral and axial resolution of a nonlinear laser scanning microscope by measuring its point spread function (PSF) in two ways: by imaging fluorescent beads using two-photon excited fluorescence (standard method), and by using monolayers of molybdenum disulfide – MoS_2 (non-standard method), obtained by chemical vapor deposition [1], which, due to the lack of central symmetry, efficiently generate second harmonic signal.

Parameters such as the numerical aperture of the objective and the excitation wavelength contribute to the resolution, so it changes depending on the current setting of the microscopic system. Measurements were performed for two different objectives and several standard excitation wavelengths, depending on the type of sample. As expected, the best resolution was obtained for the objective with the largest numerical aperture (40x 1.3) and the shortest excitation wavelength (730nm): $R_{lat} = 260nm$, $R_{ax} = 1648nm$. In addition, the values obtained by the non-standard method are closer to the theoretical values of the resolution, because the contributions of the out-of-focus signal are significantly smaller due to the two-dimensional nature of the layers. This implies that it is better to use this type of sample to determine the resolution of the microscope. The measured PSF can be further used to deconvolve the images obtained on this microscope.

Due to its properties such as large penetration depth of incident radiation and label-free imaging, as well as the possibility of obtaining 3D models, our microscope is widely used in examination of the samples of biological origin, such as: erythrocytes [2], chitinous structures [3], human colon tissue [4], collagen and dentin.

Acknowledgements: The work was funded by the Science Fund of the Republic of Serbia, within PROMIS program, through HEMMAGINERO project and by the Institute of Physics Belgrade, through the grant by the Ministry of Education, Science and Technological Development of the Republic of Serbia.. The authors would like to thank prof. Vladana Vukojevic from Karolinska Institute in Stockholm, Sweden for providing fluorescent beads.

References

1. A. Senkic *et al.*, in preparation, CVD growth parameters on global and local optical properties of MoS2 monolayer
2. K. Bukara *et al.*, J. Biomed. Opt. **22**(2), 026003 (2017)
3. MD Rabasovic *et al.*, J. Biomed. Opt. **20**(1), 016010 (2015)
4. SZ Despotovic *et al.*, Sci. Rep. **10**, 6359 (2020)

S13-BMP-201 / **Poster presentation (virtual)**

Calorimetric Tracking of the Plasma and CSF Proteome in Children With Acute Lymphoblastic Leukemia

Authors: B. Antonova[1]; K. Batchvarov[2]; Yoan Dimitrov[1]; S. Abarova[1]; B. Tenchov[1]; B. Avramova[2]; M. Jordanova[2]; D. Konstantinov[2]

[1] *Medical Faculty, Medical University – Sofia, Bulgaria*

[2] *Department of Pediatric Hematology and Oncology, University Hospital "Queen Joanna", Sofia, Bulgaria*

Presenter: Y. Dimitrov (yoandimitroff@gmail.com)

Leukemia is the most common type of cancer found in children. It accounts for around 33% of all malignant diseases in pediatrics.

Differential scanning calorimetry DSC is a highly sensitive technique that measures temperature-induced conformation changes in proteins. As such, it is useful in measuring the exact values of concentration, conformation and interaction between proteins and other molecules and allows for observing specific insignificant changes in blood plasma and CSF (cerebrospinal fluid), related to various pathological processes. This way, plasma and CSF proteins could serve as biomarkers for the diagnosis and monitoring of the disease.

In this study we have used DSC to compare alterations in the protein thermal denaturation profiles of blood plasma and CSF, taken from children with acute lymphoblastic leukemia (ALL), with the corresponding fluids from other children in continuous remission with healthy clinical and hematological statuses, used as controls.

Here we present DSC measurements of blood plasma in children in cases with leukemic infiltration present in the bone marrow. In some cases they are about newly developed disease or relapsed one, and in other cases about Non-Hodgkin's lymphoma with secondary spread to the bone marrow and also lymphoid blast crisis

Development of two-dimensional superresolution fluorescence microscope with structured illumination

A. Denčevski, A.J. Krmpot and M.D. Rabasović
Institute of Physics Belgrade, University of Belgrade, Belgrade, Serbia
e-mail: aleksa.dencevski@ipb.ac.rs

Structured Illumination Microscopy - SIM is a wide-field microscopy technique that enables imaging of biological samples with a lateral resolution better than the diffraction limit [1]. In this paper, we present a low-cost, custom-made superresolution fluorescent microscope which enables recording of images in two modes: epifluorescence mode and superresolution mode. Images taken in epifluorescence mode have a resolution that is slightly above the diffraction limit, while superresolution images are taken with a resolution significantly below the diffraction limit.

This microscope is basically a conventional epifluorescence microscope with the addition of specially designed diffraction grating. The excitation of the microscope is designed so that simultaneous imaging of samples at different excitation wavelengths is possible. An independent controlling system with microcontrollers was developed for this microscope. Controlling system was specifically designed to synchronously activate laser diodes, initialization of camera exposure, as well as a system for rotating diffraction grating, with the aim that biological samples are exposed to laser radiation only during image recording. On the other hand, the software of this microscope enables all users to quickly control all parts of the system as well as reconstruct recorded images. A significant application of this technique is in the recording of various biological samples [2], non-invasively, with minimal photobleaching and phototoxicity of the samples while using low laser power.

REFERENCES

[1] M. Saxena *et al.*, Adv. Opt. Photonics 7, 241 (2015).
[2] M. Iwai *et al.*, Plant J. 96, 233 (2018).

Cutting edge technique for determination of spatial resolution limits of nonlinear laser scanning microscopy

M. Bukumira[1], J. Jelić[1], A. Denčevski[1], M.D. Rabasović[1], N. Vujičić[2], A. Senkić[2], A. Supina[2] and A. Krmpot[1]
[1]*Institute of Physics Belgrade, University of Belgrade, Laboratory for Biophysics, Belgrade, Serbia*
[2]*Institute of Physics, Center of Exellence for advanced Materials and Sensing devices, Zagreb, Croatia*
e-mail: marta@ipb.ac.rs

Microscope resolution is the shortest distance between two points on a sample that can be distinguished as separate entities. Due to the wave nature of light and the phenomenon of diffraction, it is fundamentally limited: even under theoretically ideal conditions and optical components, the microscope has a finite resolution.
In this paper, we determined the lateral and axial resolution of a nonlinear laser scanning microscope by measuring its Point Spread Function (PSF). The measurement was preformed in two ways: by imaging fluorescent beads using two-photon excited fluorescence (standard method), and by using transition metal dichalcogenide monolayers of molybdenum disulfide and tungsten disulfide (cutting edge method). The monolayers - obtained by chemical vapor deposition [1], efficiently generate second harmonic (SHG) signal due to the lack of central symmetry. The monolayers were also used for determination of the lateral resolution of third harmonic generation (THG) microscopy.
Measurements were performed for different objectives and several standard excitation wavelengths, depending on the type of sample. As expected, the best resolution was obtained for the objective with the largest numerical aperture and the shortest excitation wavelength. In addition, the values obtained by the non-standard cutting edge method are closer to the theoretical values of the resolution, because the contributions of the out-of-focus signal are significantly reduced due to the two-dimensional nature of the layers. The measured PSF can be further used to deconvolve the images obtained on this microscope.
Due to its properties such as great depth of penetration of incident radiation and label-free imaging, as well as the possibility of making 3D models, our microscope is widely used in examining samples of biological origin, such as: erythrocytes [2], chitin structures [3], human colon [4], collagen, dentin, etc.

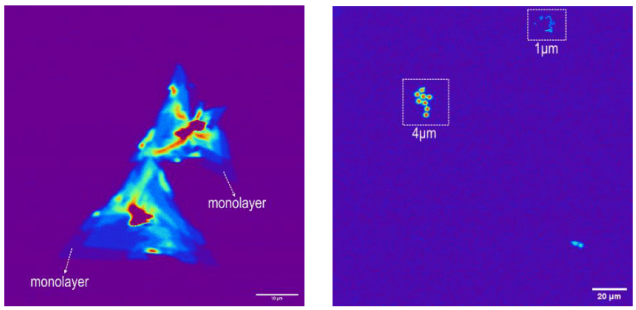

Figure 1. Left: WS_2 (mono)layers; right: fluorescent beads of different diameters (4µm and 1µm).

REFERENCES
[1] A. Senkic *et al.*, Mater. Chem. Phys. 296, 127185 (2023).
[2] K. Bukara *et al.*, J. Biomed. Opt. 22, 026003 (2017).
[3] M.D. Rabasovic *et al.*, J. Biomed. Opt. 20, 016010 (2015).
[4] S.Z. Despotovic *et al.*, Sci. Rep. 10, 6359 (2020).

P 15

Quantitative measurement of concentration and diffusion properties of molecules using fluorescence correlation spectroscopy

J. Z. Jelić, A. Denčevski, M. D. Rabasović, A. J. Krmpot

Institute of Physics Belgrade, University of Belgrade, Belgrade, Serbia

Fluorescence **C**orrelation **S**pectroscopy (FCS) is a powerful and non-invasive technique for quantitative characterization of the concentration, mobility, and interactions of fluorescent/fluorescently labeled molecules *in vitro* and *in vivo* [1]. By exploiting the capabilities of a confocal microscope and time-correlated single photon counting (TCSPC), FCS offers extremely high temporal resolution (down to picosecond time scale), diffraction-limited spatial resolution (≈ 200 nm), as well as single-molecule sensitivity. Conventional Fluorescence Correlation Spectroscopy (FCS) utilizes temporal autocorrelation analysis of fluctuations in the recorded fluorescence signal caused by the motion of molecules (concentrations in nM range) through the small sample volume, often referred to as the focal volume (typically 0.2 – 1 fL) [2]. Furthermore, FCS can provide insights into local microenvironments, such as viscosity or pH, or about any other molecular process related to alterations in the fluorescence signal. By labeling the drug or the target molecule with a fluorophore, FCS can quantify the binding affinity, association/dissociation kinetics of drug-target interactions [3].

Here, we present our custom-made Fluorescence Correlation Spectroscopy (FCS) system, which utilizes a laser diode operating at 488 nm to effectively excite fluorescent dyes such as Alexa 488, FITC, Atto 488, and Rhodamine 110. We conducted a comprehensive characterization of the system's performance by studying Rhodamine 110 in both aqueous solutions and sucrose solutions with varying mass percentages. In the case of a 2 nM aqueous solution of Rhodamine 110, we obtained a diffusion time of 30 µs. Further analysis of the obtained results clearly demonstrates that our home-built FCS system achieves single-molecule sensitivity and possesses a focal volume that is comparable to that of commercial instruments.

Acknowledgements: This work was supported by the Science Fund of the Republic of Serbia through program PROMIS [project HEMMAGINERO, grant number 6066079] and Green Program of Cooperation between Science and Industry [project BioPhysFUN, grant number 4545]. The authors would like to thank prof. Vladana Vukojević from Karolinska Insitute in Stockholm, Sweden for providing fluorescent probes.

References

[1] Haustein, E. and Schwille, P. 'Fluorescence Correlation Spectroscopy: Novel Variations of an Established Technique', Annu. Rev. Biophys. Biomol. Struct., 36 (1). (2007)

[2] Yu, L. *et al.* 'A comprehensive review of Fluorescence Correlation Spectroscopy', *Frontiers in Physics*, (2021).

[3] Delie, F., Gurny, R. and Zimmer, A. 'Fluorescence correlation spectroscopy for the characterisation of drug delivery systems', Biol. Chem., 382(3), (2001).

Одређивање границе просторне резолуције нелинеарне ласерске скенирајуће микроскопије

Марта Букумира[1], Станко Николић[2], Јована Јелић[1], Алекса Денчевски[1], Михаило Рабасовић[1], Наташа Вујичић[3], Ана Сенкић[3], Антонио Супина[3], Александар Крмпот[1]

[1]*Институт за физику – Институт од националног значаја за Републику Србију, Универзитет у Београду, Лабораторија за биофизику, Београд, Србија, marta@ipb.ac.rs*
[2]*Институт за физику – Институт од националног значаја за Републику Србију, Универзитет у Београду, Лабораторија за квантну биофотонику, Београд, Србија*
[3]*Институт за физику, Знанствени центар изврсности за напредне материјале и сензоре, Загреб, Хрватска*

Резолуција микроскопа је најкраће растојање између две тачке на узорку које је могуће разлучити као засебне ентитете. Због таласне природе светлости и феномена дифракције, она је фундаментално ограничена: чак и при теоријски идеалним условима и оптичким компонентама, микроскоп има коначну резолуцију. У овом раду, одредили смо латералну и аксијалну резолуцију нелинеарног ласерског скенирајућег микроскопа мерењем његове функције ширења у тачки (*Point Spread Function* – PSF) на два начина: снимањем флуоресцирајућих перлица техником двофотонски ексцитоване флуоресценције и коришћењем сигнала другог хармоника који потиче од монослојева молибден дисулфида (MoS_2).[1] У одређивању резолуције фигуришу параметри попут нумеричке апертуре објектива и таласне дужине побуде, па се она мења у зависности од тренутне поставке микроскопског система. Очекивано, најбоља резолуција добијена је за објектив највеће нумеричке апертуре (40x 1,3) и најкраћу таласну дужину побуде (730 nm): $\mathbf{P_{лат} = 260\ nm}$, $\mathbf{P_{акс} = 1648\ nm}$. Додатно, вредности добијене нестандардном методом су блискије теоријским вредностима резолуције, што имплицира да је за одређивање резолуције микроскопа боље користити овај тип узорка. Због својих особина као што су велика дубина продирања упадног зрачења и осликавање без бојења узорака, као и могућности прављења 3D модела, наш микроскоп налази велику примену у испитивању узорака биолошког порекла попут: еритроцита[2], хитинских структура[3], ткива хуманог колона, колагена, дентина.

1. Senkic, A., *et al.*, CVD growth parameters on global and local optical properties of MoS_2 monolayer, *in preparation*.
2. Bukara, K., Jovanic, S., Drvenica, I.T., *et al.*, 2017, J. Biomed. Opt. 22:26003.
3. Rabasović, M.D., Pantelić, D.V., Jelenković, B.M., *et al.*, 2015, J. Biomed. Opt. 20:016010.

Захвалница: *Овај рад је финансиран од стране Фонда за науку Републике Србије, програм ПРОМИС, пројекат HEMMAGINERO. Захваљујемо се проф. др Владани Вукојевић из Каролинска Института у Стокхолму, Шведска за обезбеђене флуоресцентне сфере.*

5. Потврда о уписаним докторским студијама

УНИВЕРЗИТЕТ У БЕОГРАДУ

Адреса: Студентски трг 1, 11000 Београд, Република Србија
Тел.: 011 3207400; Факс: 011 2638818; E-mail: kabinet@rect.bg.ac.rs

Београд, 26.08.2024. год
06 Број: 61203-47/ 493-24
ЈК/

На основу члана 29 Закона о општем управном поступку ("Службени гласник РС", бр. 18/2016 и 95/2018 - аутентично тумачење и 2/2023-одлука УС), а на захтев студента Алекса Денчевски, издаје се следећа

ПОТВРДА

да је Алекса Денчевски, рођен 24.02.1998. године у Краљеву, Република Србија, уписан на докторске академске студије: „Биофизика" (180 ЕСПБ) на Универзитету у Београду, у школској 2021/2022. год. Студент је уписао школску 2023/2024. годину у статусу: финансирање из буџета.

Сврха издавања потврде: на лични захтев студента.

Руководилац Службе за студије и науку

Бранка Вукелић

6. Копија диплома основних и мастер студија

Република Србија
Универзитет у Београду
Оснивач: Република Србија
Дозволу за рад број 612-00-02666/2010-04 од 12. октобра 2011.
године је издало Министарство просвете и науке Републике Србије
Физички факултет, Београд
Оснивач: Република Србија
Дозволу за рад број 612-00-02409/2014-04 од 8. септембра 2014. године је издало
Министарство просвете, науке и технолошког развоја Републике Србије

УБ

Диплома

Алекса, Ненад, Денчевски

рођен 24. фебруара 1998. године, Краљево, Република Србија, уписан школске 2016/2017. године, а дана 10. септембра 2020. године завршио је основне академске студије, првог степена, на студијском програму Примењена и компјутерска физика, обима 240 (двеста четрдесет) бодова ЕСПБ са просечном оценом 9,66 (девет и 66/100).

На основу тога издаје му се ова диплома о стеченом високом образовању и стручном називу

дипломирани физичар

Број: 11642200
У Београду, 2. фебруара 2021. године

Декан
Проф. др Иван Белча

Ректор
Проф. др Иванка Поповић

00116819

Републике Србија
Универзитет у Београду
Оснивач: Република Србија
Дозволу за рад број 612-00-02666/2010-04 од 12. октобра 2011. године је издало Министарство просвете и науке Републике Србије
Физички факултет, Београд
Оснивач: Република Србија
Дозволу за рад број 612-00-02409/2014-04 од 8. септембра 2014. године је издало Министарство просвете, науке и технолошког развоја Републике Србије

УБ

Диплома

Алекса, Ненад, Денчевски

рођен 24. фебруара 1998. године, Краљево, Република Србија, уписан школске 2020/2021. године, а дана 28. септембра 2021. године завршио је мастер академске студије, другог степена, на студијском програму Примењена и компјутерска физика, обима 60 (шездесет) бодова ЕСПБ са просечном оценом 10,00 (десет и 0/100).

На основу тога издаје му се ова диплома о стеченом високом образовању и академском називу

мастер физичар

Број: 13223800
У Београду, 1. фебруара 2022. године

Декан
Проф. др Иван Белча

Ректор
Проф. др Владан Ђокић

00132552

7. Одлука о одобреној теми докторске дисертације

УНИВЕРЗИТЕТ У БЕОГРАДУ

Адреса: Студентски трг 1, 11000 Београд, Република Србија
Тел.: 011 3207400; Факс: 011 2638818; E-mail: kabinet@rect.bg.ac.rs

Београд, 10. јула 2024. године
06 Број: 06-51/III/1634/4-24
JKJ/

На основу члана 50. ст. 4. тач. 3 Статута Универзитета у Београду Статута Универзитета у Београду („Гласник Универзитета у Београду“, број 201/2018, 207/2019, 213/2020, 214/2020, 217/2020, 230/21, 232/22, 233/22, 236/22, 241/22, 243/22, 244/23 и 245/23), а на предлог Већа за студије при Универзитету од 10. јуна 2024. године, Већа за интердисциплинарне, мултидисциплинаре и трансдисциплинарне студије на седници одржаној 10. јула 2024. године, донело је

О Д Л У К У

1. ОДОБРАВА СЕ израда докторске дисертације под насловом: **Развој суперрезолуционог микроскопа са структурисаним просветљавањем за изучавање морфолошких промена еритроцита,** кандидата **Алексе Денчевског** (докторске студије: Биофизика).

2. За менторе се именују:
1. др Михаило Рабасовић, виши научни сарадник, Институт за физику (физика)
2. др Ивана Дрвеница, виши научни сарадник, Институт за медицинска истраживања (медицина, биотехнологија)

П Р Е Д С Е Д Н И К
ВЕЋА ЗА ИМТ СТУДИЈЕ
Проф. др Дејан Филиповић